Theoretical and Applied Fracture Mechanics 120 (2022) 103423

Contents lists available at ScienceDirect

Theoretical and Applied Fracture Mechanics

journal homepage: www.elsevier.com/locate/tafmec

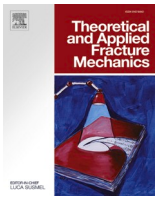

# The effect of porosity size and oxidation on the HCF property of nickel-based single crystal superalloy at 980 ℃

Wen Jiang [a,b,*], Piao Li [c], Wei-Xing Yao [c], Shao-Shi Rui [d,e], Hui-Ji Shi [e], Jie Huang [c]

[a] Nanjing Engineering Institute of Aircraft Systems, AVIC, Nanjing 211106, China
[b] Aviation Key Laboratory of Science and Technology on Aero Electromechanical System Integration, Nanjing 211106, China
[c] State Key Laboratory of Mechanics and Control of Mechanical Structures, Nanjing 210016, China
[d] LNM, Institute of Mechanics, Chinese Academy of Sciences, Beijing 100190, China
[e] AML, School of Aerospace Engineering, Tsinghua University, Beijing 100084, China

ARTICLE INFO

*Keywords:*
Nickel-based single crystal superalloys
High-cycle fatigue life
Fatigue limit
Porosity size
Oxidation

ABSTRACT

The high-cycle fatigue (HCF) lives and fatigue limits of nickel-based single crystal superalloys (NBSX) with different porosity sizes were investigated at 980 °C. The test results show that the failure cracks prone to initiate from large internal pores, and the HCF properties are mainly controlled by the critical pore size. However, when the stress is close to the fatigue limit, the secondary cracks will initiate from the oxide layer obviously, which will further weaken the HCF properties. Therefore, a life prediction model based on the critical plane parameter and oxidation kinetic equation was proposed to evaluate the effect of porosity size and oxidation on the HCF life of NBSX. Then, combing the life prediction model and Murakami model, a fatigue limit evaluation model was presented. Compared with test results, the life prediction model and fatigue limit evaluation model are accurate and effective. Finally, the defect-tolerance analysis was carried out by the Kitagawa-Takahashi diagram, which could be a visual guide for the anti-fatigue design of NBSX.

## 1. Introduction

Due to the elimination of grain boundaries, nickel-based single crystal (NBSX) superalloys have higher high-temperature strength, better creep and fatigue properties, and have been widely used in advanced aero-engines and gas turbines [1]. NBSX blades are often subjected to complex loads during services, such as high temperature, large centrifugal force, cyclic load, vibration and thermomechanical fatigue (TMF) load [2–4], which can lead to blade fatigue failure. The statistical analysis on the failure causes of military aero-engines has found that high-cycle fatigue (HCF) is the main reason accounting for blade failure. Because the fatigue cracks will initiate and propagate from small defects under high-frequency vibration, resulting in rapid and often unpredictable fatigue failure [5]. Therefore, a reasonable assessment of the pore defect influence on the HCF performance for NBSX superalloys is vital to guarantee the safety and reliability of NBSX blades. Due to the complexity of fatigue life evaluation, engineers tend to use the fatigue limit to evaluate the HCF performance in practical fatigue design [6]. The fatigue limit originally means that the S-N curve of some metallic materials has a clear lower limit in the life range of $10^6$-$10^7$ cycles. When the applied stress is lower than fatigue limit, no matter how many cycles it goes through, the specimens or structures will not fail [7]. However, this concept has been challenged under the background of the very high-cycle fatigue (VHCF), as a further drop of the S-N curve could be found after $10^8$ cycles even for metals with obvious fatigue limit in the HCF region [8]. In this paper, when the term 'fatigue limit' is used, it characterizes the stress range or amplitude when the specimens go through $10^7$ loading cycles without failure.

Currently, there are some researches on the influence factors of the fatigue limit for nickel-based superalloys. Gordeeva et al. [9] studied the effect of orientation on the fatigue strength of directionally solidified alloy ZHS6U and found that the fatigue strength of the specimen along the solidification direction was 1.5–2 times that of the specimen perpendicular to the solidification direction. Research results from Gorbovets et al. [10] also show that the orientation deviation has a great influence on the fatigue limit of NBSX superalloy, as well as the scatter of fatigue limit. Zhang and his coworkers [11] compared the fatigue limit of single crystal, directionally solidified and cast nickel-based superalloys near 800 °C. The results reveal that the NBSX superalloys have the highest fatigue limit because there are fewer pores and inclusions in

* Corresponding author at: Nanjing Engineering Institute of Aircraft Systems, AVIC, Nanjing 211106, China.
*E-mail address:* jiangwen@nuaa.edu.cn (W. Jiang).

https://doi.org/10.1016/j.tafmec.2022.103423
Received 15 February 2022; Received in revised form 12 May 2022; Accepted 30 May 2022
Available online 2 June 2022

them and their grain boundaries are eliminated. Kevinsanny et al. [12] further investigated the effect of defect size on the fatigue limit of the powder superalloy Ni-718 and discovered that the fatigue limit was dependent on the competition between grain size and defect size. Lin et al. [13] found that the higher the carbide inclusion content in the cast superalloy MAR-M247, the lower the fatigue strength. Ren and Nicholas [14] explored the influence of low-cycle fatigue (LCF) on subsequent HCF limit. Their results demonstrate that even small fractions of LCF life consumption can significantly reduce the subsequent HCF limit, and the reduction is attributed to a combination of LCF damage and the plastic deformation induced during the LCF process. Chu et al. [15] conducted HCF tests on the directionally solidified alloy DZ951 and found that the fatigue limit peaked at 700 °C. Shui and his coworkers [16] also found that the fatigue limit peaked at 700 °C in the HCF test of NBSX superalloy AM3. This is because the interaction of high temperature and cyclic stress at 700 °C would induce the precipitation of homogeneous hyperfine secondary γ′ particles, which is beneficial to fatigue limit. However, the cyclic stress would lead to the formation of persistent slip bands moving through the γ matrix channels and the γ′ precipitates at higher temperature, which promoted crack initiation and reduced the fatigue limit. Wang et al. [17] studied the difference of fatigue limit between the smooth and notched specimens of nickel-base superalloy GH4698. The results show that a single primary crack initiates on the surface or near the surface of the smooth specimen, while multiple cracks initiate on the notched surface of the notched specimen, which makes the fatigue limit of smooth specimens higher than that of notched specimens. This result is consistent with the research results from Chu et al. [15]. Filippini and his coworkers [18] considered the influence of notches on the fatigue strength of NBSX superalloy CMSX-4 through experiments and finite element methods, and the results revealed that the notch shape has a great influence on the fatigue strength. Zhong et al. [19] studied the effect of surface stress state on powder superalloy FGH4097 and discovered that a stable residual compressive stress would remain on the specimen surface after spray strengthening, which effectively improved the crack initiation resistance and significantly increased the fatigue limit.

The existing literature mainly studies the influence factors of the fatigue limit for nickel-based superalloys through experiments and a lack of quantitative evaluation model for the influence of defect size on the fatigue limit of NBSX superalloys still exists. The experimental results [20–24] demonstrate that for most of the NBSX specimens, failure cracks initiate at the porosity defects, and the porosity defect size is the main factor controlling the HCF lives of NBSX superalloys. However, near $10^6$-$10^7$ cycles, the appearance of surface oxide layer will further weaken the fatigue properties of NBSX superalloys [20,25],especially when the temperature is over 900 °C, the thickness of the surface oxide layer increases significantly [26]. Therefore, it is necessary to develop a quantitative model to evaluate the effect of porosity size and oxidation on the fatigue limit of NBSX superalloys at a high temperature.

For polycrystalline metals (such as cast iron, aluminum alloy and 3D printing alloy, etc.), defect-tolerance design [6] assumes that small defects act as effective crack initiators and that non-propagating cracks associated with these defects are always present at or slightly below the fatigue limit, which has been widely used to evaluate the effect of randomly distributed defects on the fatigue limit. For example, the Murakami model [27] takes micro-hardness, critical defect size and critical defect location as parameters to evaluate the fatigue limit of materials, which is easy to obtain parameters and convenient for engineering applications. It is generally considered [28] that when the defect size is smaller than the safety defect size, it will not have a detrimental impact on the fatigue performance. When the defect size exceeds the safety defect size, the fatigue limit decreases with the increase of the defect size. The Kitagawa-Takahashi (K-T) diagram [29,30], which combines the fatigue limit and fracture mechanics in a semi-empirical way, can describe the change of fatigue limit with critical defect size. Moreover, the K-T diagram can determine the safe (infinite) life region for non-propagating cracks. The specimens within the region are considered to have infinite life (more than $10^7$ cycles), while specimens outside the region will fail before $10^7$ cycles. So the K-T diagram can directly and conveniently guide the engineering fatigue design. However, it still needs to study whether the above defect-tolerance design method is suitable for NBSX superalloys at high temperatures.

Based on this background, the main purpose of this paper is to quantitatively evaluate the effect of porosity size and oxidation on the HCF life and the fatigue limit of NBSX superalloys at high temperatures. It should be pointed out that, when HCF load applies, the NBSX superalloys experience serious TMF damage at the same time. As the TMF damage lies in the LCF range [4], when studying the HCF life and fatigue limit of NBSX, the TMF load is not considered in this paper. In addition, the orientation deviation also has negative effect on the fatigue performance of NBSX [31]. In order to reduce the research complexity, the coupling influence of pore size and orientation deviation is not considered here and will be studied in future research. In our previous work [32], two groups of specimens with different pore size distributions were used to carry out the HCF tests at 980 °C, and the effect of pore size on HCF life was quantitatively evaluated. On this basis, the fatigue tests with lower stress levels under the same test conditions were conducted, and the fatigue limits of two groups of specimens are obtained by the staircase method. Then, a fatigue life prediction model considering the porosity size and oxidation was presented. The defect-tolerance analysis is carried out by the K-T diagram, which including putting forward a classical safe-life region, as well as the porosity defect and oxidation determined life distribution in the finite-life region. Finally, based on the Murakami model, a new model was proposed to evaluate the fatigue limit of NBSX superalloy, which considered the effect of porosity size and oxidation.

## 2. Experiment

### 2.1. Material and specimens

The second-generation NBSX superalloy DD5, manufactured by the Institute of Metal Research, Chinese Academy of Sciences, has been used in the experiment. Its nominal chemical composition is detailed in Table 1. The single-crystal bars were prepared by a vacuum directional solidification method with a selector technique, and the expected axial orientation is [0 0 1]. However, there is usually a certain deviation after directional solidification between the actual crystal orientation and the expected orientation of specimen and real blade structure [33], and this misorientation can cause performance differentiation. In industrial production, in order to ensure the quality and performance of blades, the orientation deviation angle is generally required to be less than 15° [34]. Our previous research also shows that the effect of small misorientation (<15°) on the fatigue properties of NBSX is smaller than that of fatigue scatter [35]. So the misorientation is as required within 15° in this paper. The effect of misorientation will be considered through the life scatter band rather than a specific model parameter. For all specimens, the heat treatments [36]: were given as follows: a two-step solution treatment by 1310 °C × 2 h + 1313 °C × 2 h (air cooling), and a two-step aging treatment by 1130 °C × 4 h + 870 °C × 16 h (air cooling). The heat treatment was performed in a vacuum furnace with temperature fluctuation within ± 5 °C.

Two groups of DD5 specimens with different porosity sizes were manufactured for fatigue tests. The specimens with large pores are classified into the LP group, while the specimens with small pores are classified into the SP group. The dimension and configuration of HCF specimens are shown in Fig. 1. The hourglass-shaped HCF specimens have a total length of 70 mm and the gauge diameter is ~5 mm. After turning and precision polishing, the surface roughness *Ra* of HCF specimens is 0.4 μm.

**Table 1**
Nominal chemical composition of DD5 (in wt. pct.).

| Element | Ni | Cr | Co | Mo | W | Ta | Re | Hf | Al | C | B | Y |
|---|---|---|---|---|---|---|---|---|---|---|---|---|
| Wt. Pct. | Bal. | 7 | 8 | 2 | 5 | 7 | 3 | 0.2 | 6.2 | 0.05 | 0.04 | 0.01 |

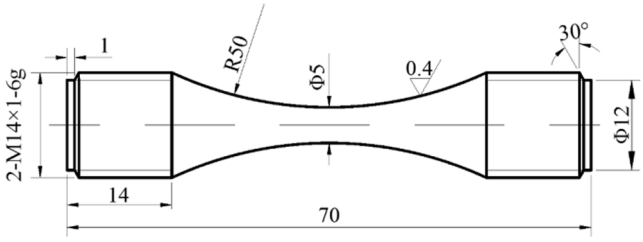


**Fig. 1.** The dimensions and configuration of specimens (mm).

### 2.2. Microstructure and hardness

Mirror polished samples were prepared from fully heat-treated single-crystal bars (7.5 mm in radius), along the cutting plane of ~[001] and perpendicular to the solidification direction. Then the size and spatial distribution of porosity defects were analyzed by the metallographic method [32]. The average porosity area fraction of the SP sample was 0.19% and that of the LP sample was 0.14%. The pore defects inside the sample (especially within the radius of 2.5 mm) are more concentrated, and the largest pores are likely to appear there.

Recently, the Feret diameter $\phi_{surr}$ was proposed in [37] as an equivalent pore size definition in terms of its severity in fatigue and as an alternative to $\sqrt{area}$. Due to the complexity of pore shape in the 3-D structure, the size of the pore observed by 2-D metallography may be 2–3 times smaller than the actual size [38], so the commonly used $\sqrt{area}$ will make the result smaller. The Feret diameter is defined as the circumscribed circle diameter of pore defect in a 2-D view and it can lead to a conservative result, which could be more in line with the reality. Therefore, the Feret diameter $\phi_{surr}$ was used to describe the size of pore defects. The pore size distributions are shown in Fig. 2. The statistical results show that the pore size distributions of SP and LP specimens are similar, which can be well characterized by log-norm distribution, and 85% of the pores are distributed in the range of 10–20 μm. However, there is a slight difference in the distribution of the tail part, which is mainly due to the fact that the observed largest pores of SP samples are smaller than that of LP samples. The statistical extremum value (SEV) method [39] was used to evaluate the maximum pore size of specimens, and the estimated maximum pores size of SP and LP specimens are 153 μm and 231 μm respectively.

The hardness in [001] direction of 12 metallographic samples in each group of specimens was measured by high temperature hardness tester AVK-HF at 980 °C, and the hardness of each sample was measured at 5 sites on a straight line. The measurement results show that the hardness of SP and LP samples are almost the same, the average Vickers hardness of the SP and LP specimens are respectively 455.5 kgf/mm$^2$ and 448.9 kgf/mm$^2$.

### 2.3. Fatigue resistance tests

The HCF tests were carried out on the high frequency testing machine QBG-50B (Fig. 3**(a)**), and controlled by a constant-amplitude sinusoidal loading. The tests were performed in air under the temperature of$T$ = 980°C, the loading frequency of$f$ = 110 Hz, and the stress ratio of$R$ = 0.1. A high-temperature furnace with resistance wires evenly distributed inside (Fig. 3**(b)**) was used to heat the specimens. The temperature was measured by a thermocouple (Fig. 3**(c)**) which was fixed on the specimen, and the temperature error was within 3 °C. To ensure that the surface and internal temperature of the specimens are consistent, the fatigue tests were carried out only after the specimen had been slowly heated for one hour and then kept heated for another hour.

The HCF tests were performed under four stress levels (560 MPa, 640 MPa, 710 MPa and 765 MPa) in previous work [32], and the test results are given in the first 13 rows of Table 2 and Table 3. The fatigue failure criterion is defined as complete failure and fracture. In this paper, the fatigue tests with lower stress levels under the same test conditions were conducted, and the main purpose of tests is to obtain the fatigue limit. The fatigue limit was measured by the staircase method and the runout limit was set to be $10^7$ cycles. The staircase method [40] was first proposed by Dixon and Mood, and then commonly used to determine the fatigue limit [28]. This method assumes that the fatigue limit obeys the normal distribution, so the maximum likelihood estimation of the mean value of fatigue limit is carried out through the up and down of fatigue stress.

After the fatigue tests, the fatigue fracture analysis was carried out on

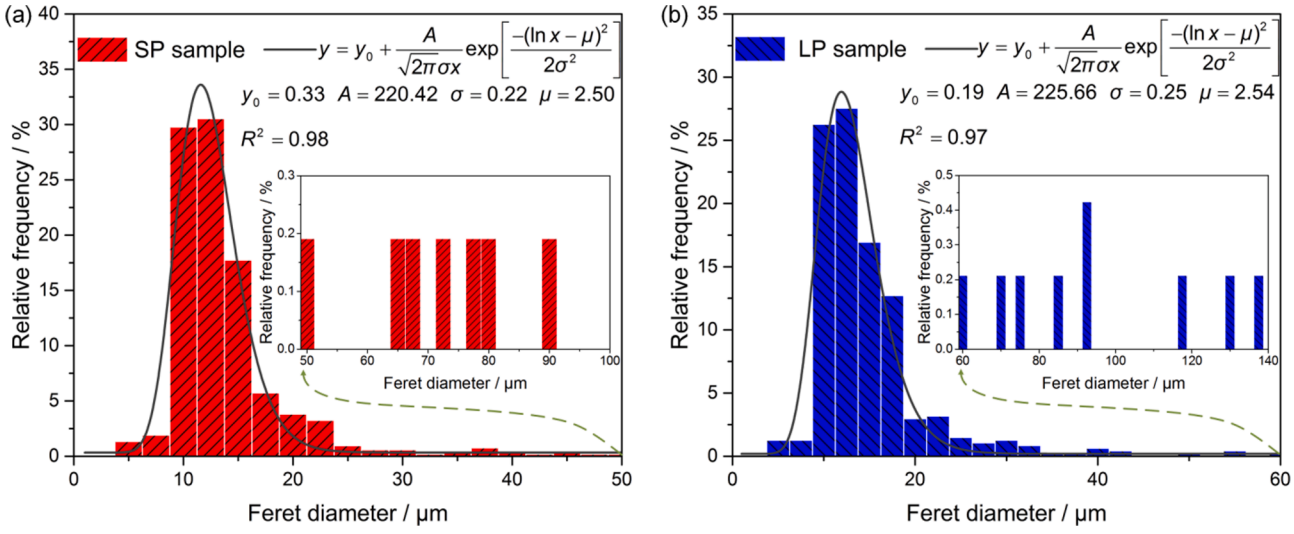


**Fig. 2.** The porosity defect size distribution of (a) SP sample, (b) LP sample [32].

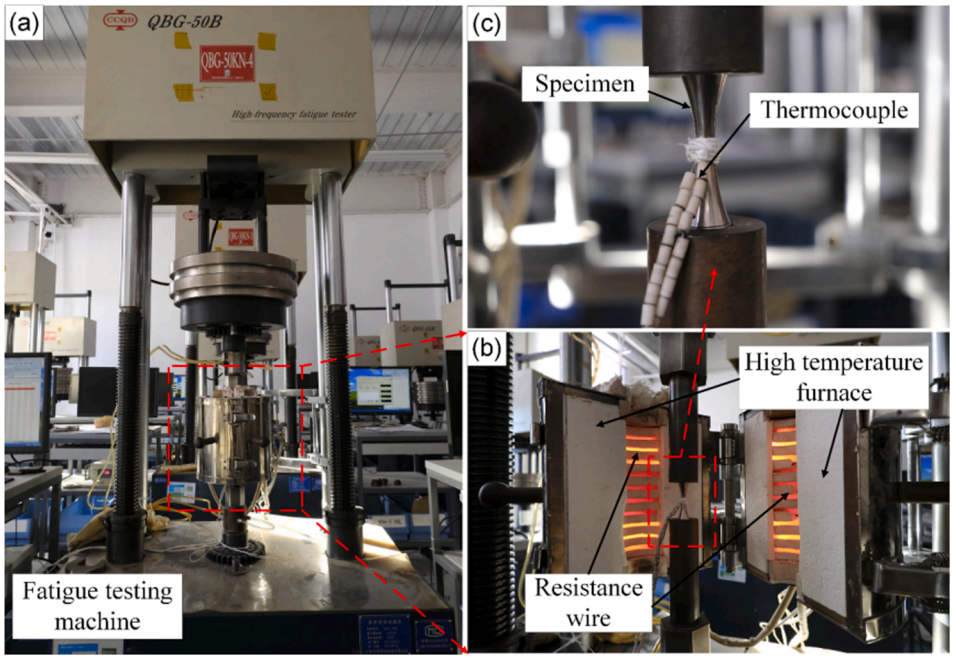


**Fig. 3.** The schematic diagram of test equipment: (a) Fatigue testing machine, (b) Heating and holding device, (c) Temperature control device.

**Table 2**
Fatigue resistance test results of SP group.

| Reference | $\sigma_{max}$/MPa | $N_f$ | Failure crack initiation site | $\phi_{surr}$/μm | $\phi_{surr}/d$ |
|---|---|---|---|---|---|
| SP-1 | 765 | 130,000 | Internal pore | 96.6 | 0.06 |
| SP-2 | 765 | 113,000 | Internal pore | 103.1 | 0.10 |
| SP-3 | 765 | 198,000 | Internal pore | 90.4 | 0.12 |
| SP-4 | 710 | 202,000 | Internal pore | 120.5 | 0.08 |
| SP-5 | 710 | 343,000 | Internal pore | 92.7 | 0.10 |
| SP-6 | 710 | 482,000 | Internal pore | 72.6 | 0.11 |
| SP-7 | 640 | 701,000 | Internal pore | 77.7 | 0.01 |
| SP-8 | 640 | 1,768,000 | Internal pore + Oxide layer | 44.6 | 0.02 |
| SP-9 | 640 | 2,186,000 | Oxide layer | / | / |
| SP-11 | 560 | 1,120,000 | Internal pore + Oxide layer | 142.1 | 0.06 |
| SP-12 | 560 | 2,572,000 | Internal pore + Oxide layer | 90.1 | 0.05 |
| SP-13 | 560 | 2,876,000 | Oxide layer | / | / |
| SP-15 | 560 | 3,092,000 | Internal pore + Oxide layer | 103.2 | 0.13 |
| SP-16 | 500 | 7,005,000 | Internal pore + Oxide layer | 137.5 | 0.20 |
| SP-17 | 480 | >15,000,000 | / | 43.4 | 0.22 |
| SP-18 | 500 | 14,229,000 | Internal pore + Oxide layer | 59.3 | 0.13 |
| SP-19 | 520 | 11,518,000 | Internal pore + Oxide layer | 42.9 | 0.03 |
| SP-20 | 540 | 7,765,000 | Internal pore + Oxide layer | 80.4 | 0.04 |
| SP-21 | 520 | 3,361,000 | Internal pore + Oxide layer | 105.8 | 0.06 |
| SP-22 | 500 | >10,000,000 | / | 84.4 | 0.18 |
| SP-23 | 520 | 8,077,000 | Internal pore + Oxide layer | 82.8 | 0.05 |
| SP-24 | 500 | >10,000,000 | / | 68.6 | 0.16 |
| SP-25 | 520 | >10,000,000 | / | 72.3 | 0.09 |
| SP-26 | 540 | >10,000,000 | / | 46.6 | 0.14 |

**Table 3**
Fatigue resistance test results of LP group.

| Reference | $\sigma_{max}$/MPa | $N_f$ | Failure crack initiation site | $\phi_{surr}$/μm | $\phi_{surr}/d$ |
|---|---|---|---|---|---|
| LP-1 | 765 | 4,2000 | Internal pore | 124.0 | 0.10 |
| LP-2 | 765 | 5,4000 | Internal pore | 120.0 | 0.23 |
| LP-3 | 765 | 3,6000 | Internal pore | 140.2 | 0.36 |
| LP-4 | 710 | 151,000 | Internal pore | 108.5 | 0.37 |
| LP-5 | 710 | 174,000 | Internal pore | 112.7 | 0.12 |
| LP-6 | 710 | 116,000 | Internal pore | 118.9 | 0.60 |
| LP-7 | 640 | 959,000 | Internal pore | 134.1 | 0.15 |
| LP-8 | 640 | 421,000 | Internal pore | 182.0 | 0.11 |
| LP-9 | 640 | 1,168,000 | Internal pore | 107.0 | 0.13 |
| LP-10 | 560 | 6,012,000 | Oxide layer | / | / |
| LP-11 | 560 | 2,989,000 | Internal pore | 108.3 | 0.15 |
| LP-12 | 560 | 5,342,000 | Internal pore + Oxide layer | 116.1 | 0.26 |
| LP-13 | 560 | 3,905,000 | Internal pore | 120.9 | 0.22 |
| LP-14 | 490 | 8,994,000 | Internal pore + Oxide layer | 102.2 | 0.35 |
| LP-15 | 470 | 13,330,000 | Internal pore + Oxide layer | 86.7 | 0.14 |
| LP-16 | 490 | 7,371,000 | Internal pore + Oxide layer | 115.6 | 0.10 |
| LP-17 | 470 | 9,276,000 | Oxide layer | / | / |
| LP-18 | 450 | >10,000,000 | / | 70.6 | 0.22 |
| LP-19 | 490 | 6,029,000 | Internal pore + Oxide layer | 127.5 | 0.13 |
| LP-20 | 470 | >10,000,000 | / | 93.5 | 0.18 |
| LP-21 | 490 | 13,204,000 | Internal pore + Oxide layer | 89.7 | 0.14 |
| LP-22 | 510 | 9,642,000 | Oxide layer | / | / |

the field emission scanning electron microscope (FSEM) HITACHI Regulus8220, the optical microscope (OM) VHX-1000 3-DVM and scanning elec-tron microscope (SEM) TM3000 to identify the damage mechanism, the size and position of critical pores, as well as the element analysis (EDS) of oxidation crack. The critical pore means the pore where the failure crack initiates.

## 3. Results and discussions

### 3.1. Results of fatigue tests

Experimental work by Murakami [39] has revealed that the smaller the defect size in the material, the greater the fatigue limit. Fig. 4 shows the stress up-and-down diagram of SP and LP specimens. The failure specimen means failure before $10^7$ cycles, and the runout specimen

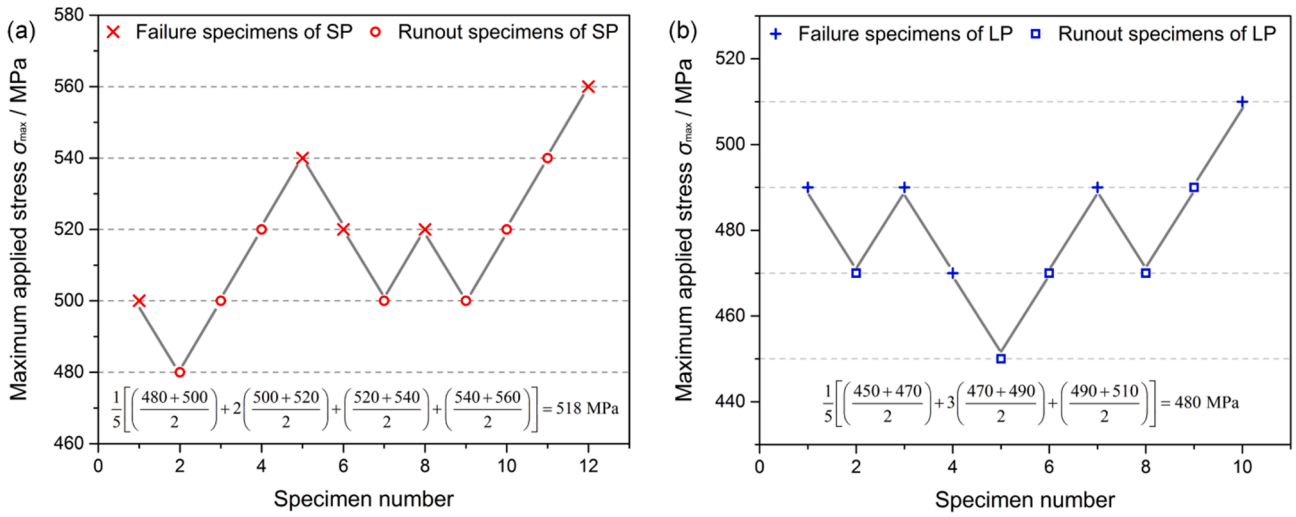


**Fig. 4.** The stress up-and-down diagram of SP group and LP group specimens.

means not fail before $10^7$ cycles. From the stress up-and-down diagram, the fatigue limits of SP and LP specimens are 518 MPa and 480 MPa respectively. As expected, the fatigue limit of the specimen with a smaller pore (SP) is higher than that of the specimen with a larger pore (LP).

The detailed test results of the two groups of specimens are respectively listed in Table 2 and Table 3, including the applied maximum stress$\sigma_{max}$, the number of cycles to failure$N_f$, the failure crack initiation site, the critical pore size$\phi_{surr}$, the distance between the main crack initiation site and the specimen surface $d$ (which can be calculated by using the section radius of the specimen minus the center distance between the circumscribed circle of the pore and the specimen section), the Murakami parameter $\phi_{surr}/d$ and its classification ($\phi_{surr}/d \geq 1.6$ for close-to-surface pore and $\phi_{surr}/d < 1.6$ for internal pore) [6].

To obtain the failure crack initiation information, the termination condition of some surviving specimens was increased to $1.5 \times 10^7$ cycles. For the specimens without fracture in the fatigue test at 980 °C, additional fatigue tests with 10% increase of loading at room temperature were then continued on the MTS 370.10 test machine until fracture, which was used to characterize the size and location of the critical pore size. From the tables, it can be seen that the failure crack initiates at internal large pore under high stress, and the failure crack initiates from the internal large pore and the surface oxide layer as the stress decreases. Only in five specimens the failure cracks initiate directly from the surface oxide layer.

According to the HCF test results in Table 2 and Table 3, the complete HCF S-N curve is shown in Fig. 5. In the double logarithmic coordinate, the S-N curve presents a three-stage feature. The first stage of the curve is a long straight descent line, followed by a short and sharp descent transition stage, and the third stage is a straight descent line again. The S-N curves of the SP and LP specimens are parallel to each other. Under the same stress level, the fatigue life of LP group with larger pores is generally lower than that of SP group with smaller pores. However, in the transition stage, the life of SP group may be slightly lower than that of LP group. Because the SP group enters the transition stage earlier and its life decreases sharply earlier.

The three-stage feature of S-N curve is due to the transition of crack initiation mode. The linear stage under high stress is dominated by pure porosity initiation (PPI) mode, while the linear stage under low stress is dominated by porosity and oxide layer co-initiation (POI) mode. In the middle transition, both of the two initiation modes may occur (mixed initiation mode). With the decrease of stress, the PPI mode gradually transits to the POI mode. The crack initiation mode will be discussed in Section 3.2.

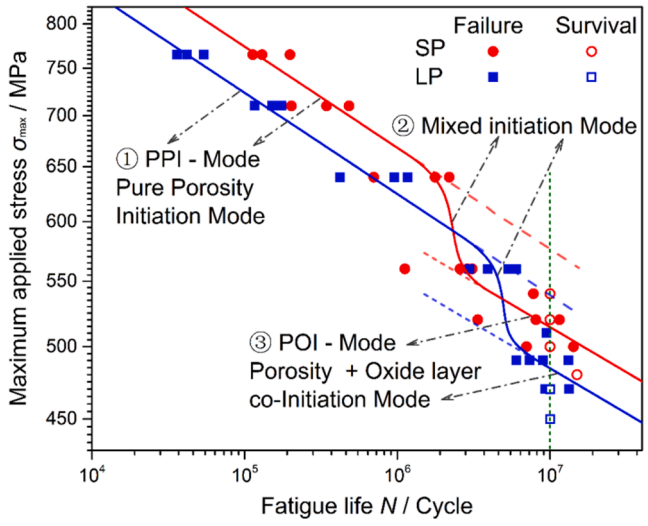


**Fig. 5.** The S-N curves of SP and LP specimens. Test data in **Appendix A** is also included.

The power law is used to fit the first and third stages of S-N curve. The fitting results and reference fatigue limit are shown in Table 4. The fitting results of PPI mode dominant curve are better, but the fitting results of POI mode dominant curve (especially LP group) are worse.

**Table 4**
Power law fitting ($\sigma_{max} = a \times N^b$) for the S-N curves, where $a$ and $b$ are fitting parameter.

| Reference | Initiation mode | Power law fitting curves | Correlation factor $R^2$ | Fatigue strength $\sigma_w$ |
|---|---|---|---|---|
| SP | PPI-Mode | $\sigma_{max} = 1617.1 \times N^{-0.064}$ | 0.91 | 576 (reference) |
| | POI-Mode | $\sigma_{max} = 1289.2 \times N^{-0.057}$ | 0.74 | 518 (experimental) |
| LP | PPI-Mode | $\sigma_{max} = 1512.0 \times N^{-0.064}$ | 0.97 | 539 (reference) |
| | POI-Mode | $\sigma_{max} = 1214.2 \times N^{-0.057}$ | 0.32 | 480 (experimental) |

Because the amount of test data in the third stage of S-N curve is small and the test data has large scatters. The test data of LP group in the third stage is concentrated around $10^7$ cycles, which is difficult to be accurately described by fitting. However, it is highly possible that the third stages of S-N curve for SP and LP groups are still parallel, so the same curve slope as SP group is used for LP group.

### 3.2. Fracture surface analysis

The typical fractured specimens under different stress levels are shown in Fig. 6. It is notable that the stress level has a direct influence on the fracture mode. Under the high stress of 765 MPa, the fracture mode is dominant by macroscopic crystallographic failure, and the fracture surface is composed of small type I crack and several {1 1 1} facets, which are at an angle of 45° with the loading direction. At 560–710 MPa, the fracture surface shows a transition from crystallographic to macroscopic type I failure, with a relative flat platform in the middle (perpendicular to loading direction) and several {1 1 1} facets surrounded. Under 530 MPa, the type I failure is predominant, and the fracture surface is approximately perpendicular to the loading direction.

This section focuses on the analysis of typical fracture surfaces in different stages of S-N curve, to identify the damage mechanism and explain the reason for the transition of the S-N curve. The typical optical microscope fractography with different crack initiation modes are shown in Fig. 7. At the first stage of the S-N curve, the failure crack initiates from a large internal pore (as shown in Fig. 7**(a)**). This failure crack initiation mode is defined as pure pore initiation (PPI) mode. At the second stage of the S-N curve, the surface oxide layer induced secondary cracks begin to appear (as shown in Fig. 7**(b)**), while the main failure crack still initiates from internal pores. This failure crack initiation mode is defined as Pore and oxide layer co-initiation (POI) mode. At the transition stage between the first and second stages of the S-N curve, the failure crack initiation mode may be PPI mode or POI mode, which is defined as mixed initiation (MI) mode. In a few cases at low applied stress, the main cracks can also initiate directly from the surface oxide layer (as shown in Fig. 7**(c)**). This failure crack initiation mode is defined as oxide layer initiation (OI) mode. Different crack initiation modes will be further discussed below.

(I). Pure pore initiation (PPI) mode

As shown in Fig. 8, due to the large size of internal pore defects, the failure crack only initiates from an internal large pore at the first stage of S-N curve. This crack initiation mode controlled by the internal critical pore size is very similar to the research results from Steuer et al. [41] in LCF, Lamm and Ormastroni et al. [20] in HCF, Cevellon et al. [22,23] in VHCF, and Kirka et al. [42] in in-phase (IP) TMF. The internal failure crack initiation firstly started from an internal pore with large size and irregular shape (see Fig. 8**(b)** and Fig. 8**(d)**), the failure crack would propagate slowly along the mode-I crack (see Fig. 8**(a)** and Fig. 8**(c)**). The slow propagation zone was relatively flat and round. The locations of the critical pores were usually in the center of the slow propagation zone. With the decrease of applied stress, the test life becomes longer and the area of slow propagation zone increases. Subsequently, the failure crack would enter the fast propagation stage. Because the crack path begins to transit from Mode I opening to crystallographic shearing along the octahedral slip planes [43], the shape of the fast propagation zone was irregular and cleavage appeared on the surface (see Fig. 8**(e)**). The final fracture zone showed a classic crystallographic fracture formed by {1 1 1} facets. From Fig. 7**(a)**, Fig. 7**(c)** and Fig. 8**(f)**, the {1 1 1} facets are relatively smooth polygon at an angle of 45° from the loading direction.

(II). Pore and oxide layer co-initiation (POI) mode

The third stage of S-N curve is dominated by pore and oxide layer co-initiation mode. As shown in Fig. 9**(a)**, when the primary crack initiates from the internal pore defect, obvious surface secondary cracks also initiate from the surface oxide layer. Different from polygon {1 1 1} facets, the shape of the surface secondary cracks (see Fig. 7**(b)** and Fig. 9**(a)**) are relatively round. Due to oxide adhesion, the color of the surface secondary crack zone(see Fig. 7**(b)**) is obviously different from that of the internal crack. This observation is consistent with the research results at similar temperatures from Ormastroni [20] and Wright [44]. Similar to the fracture surfaces of PPI mode, the primary failure crack of POI mode also initiates from an internal large pore (see Fig. 9**(b)**) and then propagates to form a large round mode-I crack. The morphology of the fast propagation zone and the final fracture zone of POI mode is also similar to the PPI mode. Different from the PPI mode, with the increase of the exposure time at high temperature, a certain thickness of oxide layer appears on the surface of POI mode dominated specimens. Subsequently, the local oxide layer could be broken and peeled off by the cyclic loading, which exposes the fresh surface to the air and high temperature again, and then multiple oxidation-induced cracks will corrode from the local oxide layer to the inside of specimens (see Fig. 9**(c)**).

The oxidation-induce cracks together with the oxide layer can be regarded as a surface defect. When they corrode to the propagation threshold, the secondary cracks will propagate from the oxide layer and form a surface slow propagation zone (see Fig. 9**(a)**). The striations and

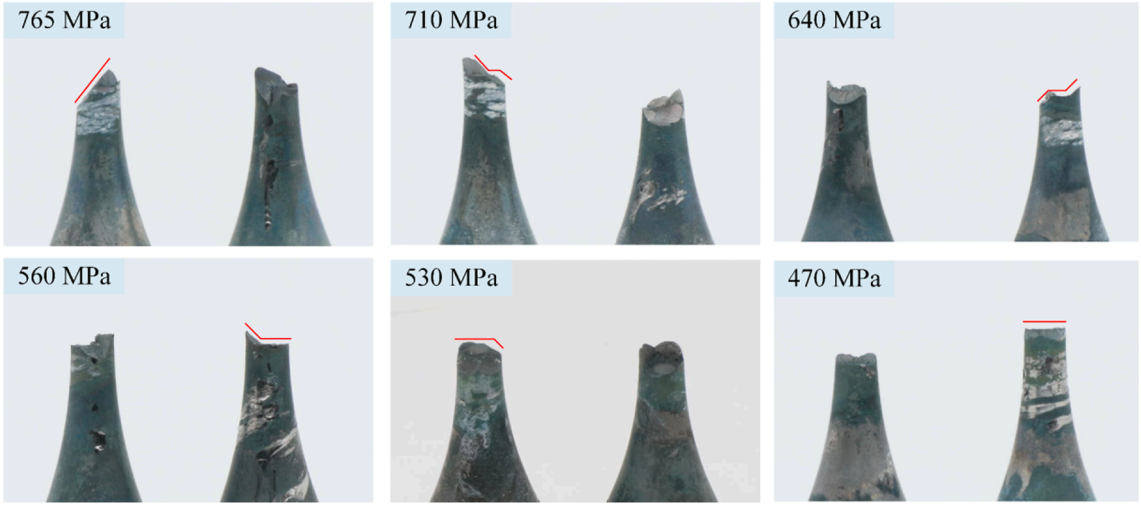


**Fig. 6.** The macro fracture morphology of specimens under different stress levels.

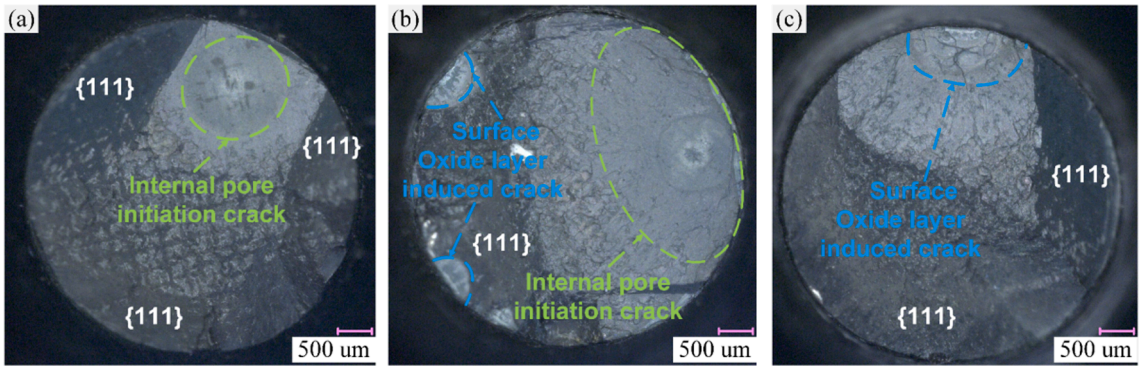


**Fig. 7.** Optical microscope fractography with different crack initiation mode. (a) PPI mode, (b) POI mode, (c) OI mode.

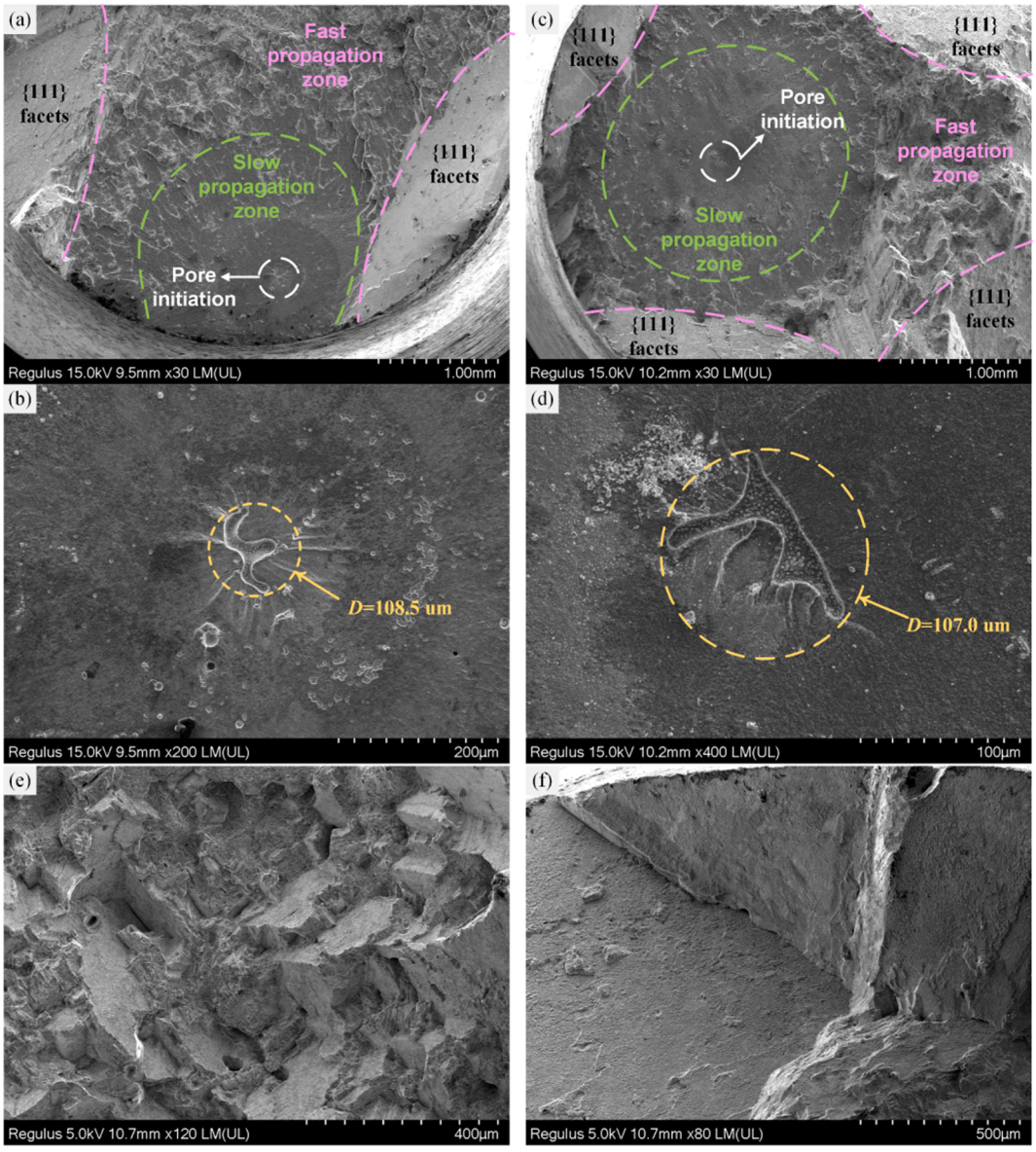


**Fig. 8.** Typical fracture surfaces of pure pore defect initiation mode. (a) and (c) are the typical fracture surfaces, (b) and (d) are the pore initiation sites of (a) and (c), (e) and (f) are respectively the magnified view of fast propagation zone and final fracture zone.

propagation direction are shown in Fig. 9**(c)** and Fig. 9**(f)**. Zhao et al [45]. also found striations in the oxidation induced crack on the surface of DD6 NBSX. Along with the surface secondary crack propagation, the oxidation-induced crack will keep on corroding to the interior of specimens. From the fracture surface, the propagation depth of the secondary crack propagation zone and the oxidation-induced crack is almost

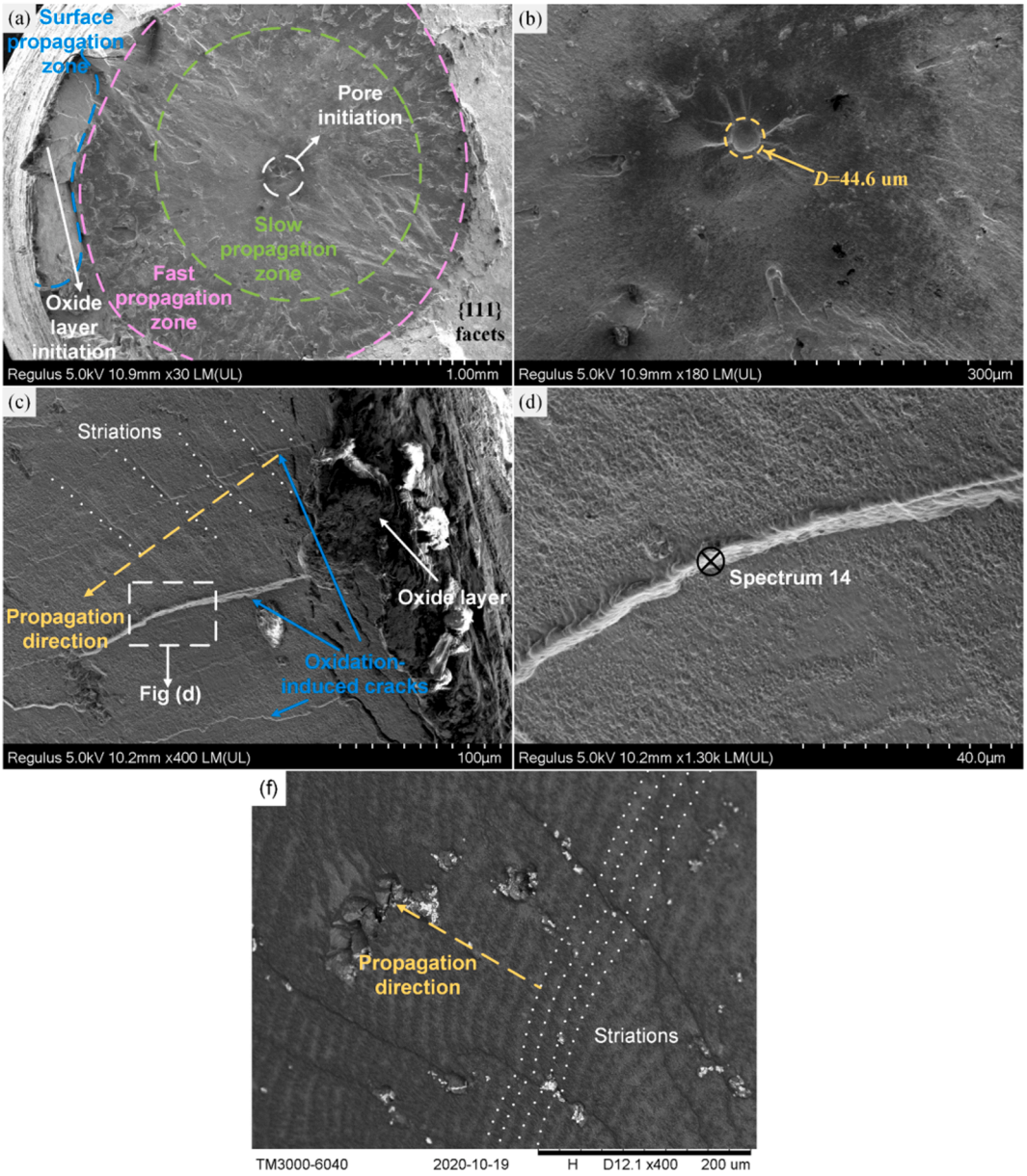


**Fig. 9.** Typical fracture surface of pore defect initiation + oxide layer initiation mode. (a) is the typical fracture surface, (b) is the pore initiation site, (c) is the surface propagation zone, and (d) is the high magnification view of the oxidation-induced crack in (c), (f) is the magnification view of striations.

the same, and their propagation depth increases with the increase of fatigue time. The surface crack in Fig. 9**(d)** is full of oxides and its element analysis was carried out in Fig. 9**(d)**. As seen in Fig. 10, the oxidation-induced crack mainly consists of O, Al, Ni, Cr, and Co, indicating the formation of $Al_2O_3$, NiO, $Cr_2O_3$, and $Co_3O_4$, which is similar to the previous observations in Karabela's research [46]. It can be seen from the fracture surface, the slow propagation zones of the internal main crack (the green area in Fig. 9**(a)**) and those of oxidation-induced secondary cracks (the blue areas in Fig. 9**(a)**) do not show interconnection, and the internal slow propagation zone is much larger than the surface propagation zones. This reflects the fact that the porosity defect and oxidation have no coupling influence on fatigue life. From the fracture surface (Fig. 7**(b)** and Fig. 9**(a)**), the propagation depth of the oxidation-induced secondary crack is much smaller than the internal crack size, the area of surface secondary crack is much smaller than that of internal crack. As the final fracture is directly related to the reduction of bearing area, the internal crack should contribute more to fatigue damage. Therefore, in spite of the surface secondary crack, the fatigue

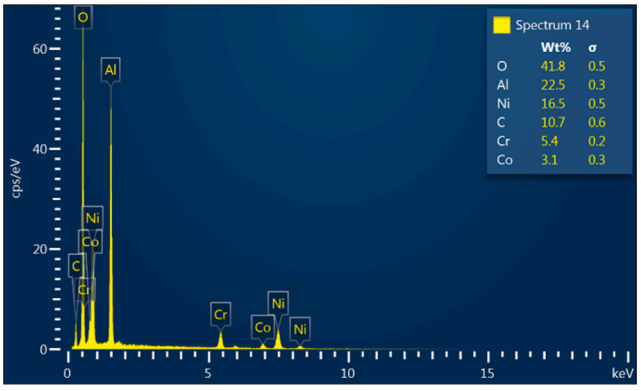


**Fig. 10.** The EDS results of the oxidation-induced crack and the scanning sites are marked in Fig. 9**(d)**.

life is still dominated by large porosity defect.

(III). Mixed initiation (MI) mode

The specimens in the transition stage of S-N curve is a mixed initiation mode, both PPI mode and POI mode are possible to appear. With the decrease of applied stress, the exposure time at high temperature increases and the PPI mode gradually transits to the POI mode.

It is known from the previous analysis that only when the corrosion depth of oxidation-induced crack reaches the propagation threshold, the surface secondary crack will propagate from the oxide layer. At high applied stress, the fatigue life is short and the depth of oxidation-induced crack is obviously less than the propagation threshold, which has little effect on the fatigue life. In the transition stage, the corrosion depth of oxidation-induced crack continues to increase and reaches the propagation threshold, then the surface secondary crack begins to propagate. Due to the scatters of oxidation performance of individual specimens, the corrosion time to reach the propagation threshold is slightly different, so the mixed initiation mode appears in the transition stage. The appearance of the surface propagation zone reduces the bearing area of the specimen, which will further weaken the fatigue performance.

As shown in Fig. 11, the oxide layer induced crack propagation rate increases with the increase of stress intensity factor (SIF), and the curve can be divided into three regions [7]. This curve is often used to explain the propagation behavior of long cracks. Before reaching the threshold, oxidation induced crack is regarded as a small crack, and its propagation is controlled by oxidation kinetics. When the oxidation induced crack propagates to a long crack and reaches the threshold, the crack propagation rate of oxidation induced crack is described by Fig. 11. In region 1, the crack propagation rate is small but increases rapidly. The crack propagation rate increases slowly in region 2, which can be described by the Paris law. Finally, the crack propagation rate near the fracture region (region 3) increases rapidly. In the PPI stage of S-N curve, the fatigue life is short and the surface oxide induced crack cannot propagate to the threshold. In this case, the non-propagating oxidation induced crack has no effect on the shape of S-N curve. When the applied stress decreases, the S-N curve enters the transition stage and the fatigue life increases. In this case, the surface oxidation induced cracks have the opportunity to expand to the threshold. Because the applied stress in the transition stage of S-N curve is relatively large, the stress intensity factor increases rapidly after the surface secondary crack reaches the propagation threshold. The surface crack will rapidly propagate to the region 2,

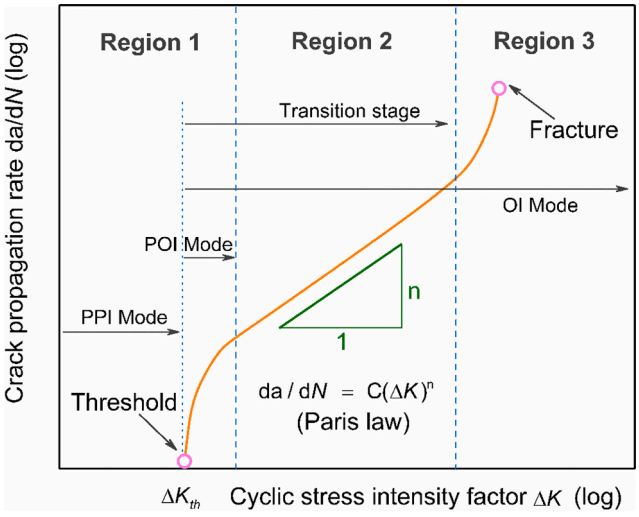


**Fig. 11.** The da/d*N*-Δ *K* diagram for describing the propagation of the oxide layer induced crack.

which brings a significant decrease to the fatigue life in the transition stage. As the applied stress continues to decrease, the S-N curve enters the POI stage. In this case, lower stress leads to lower SIF. The surface crack propagation rate is low and the surface crack propagation remains in the threshold region until fatigue failure, which makes the slope of the POI stage of S-N curve lower than that of the transition stage. Whether Fig. 11 is suitable for describing the behavior of oxidation induced crack propagation needs further quantitative research and only qualitative discussion is made in this paper.

(IV). Oxide layer initiation (OI) mode

As shown in Fig. 12, in all the HCF test specimens, failure cracks in five specimens initiated directly from the oxide layer. Wright et al. [44] also observed this phenomenon in the HCF test. It can be seen from Fig. 12**(a)**, the fracture surfaces of OI mode can be divided into oxidation zone, slow propagation zone, fast propagation zone and final fracture zone. The oxidation zone can be distinguished clearly from the slow propagation zone, as the color difference is obvious. The crescent-shaped slow propagation zone is flat, the maximum depth of oxidation-induced crack is nearly the same as that of the slow propagation zone. Due to oxide adhesion, the color of the surface secondary crack zone (see Fig. 7**(c)**) is obviously different from that of the internal crack. Fig. 12**(c)** and Fig. 12**(d)** are the high magnification view of the oxidation-induced crack in Fig. 12**(a)**, it can be seen from the figures that the cracks are filled with feather oxides. The element analysis of oxidation-induced crack in Fig. 12 was carried out in Fig. 12**(d)**. As seen in Fig. 13, the oxidation-induced crack mainly consists of O, Al, Ni, Cr, and Co, indicating the formation of $Al_2O_3$, NiO, $Cr_2O_3$, and $Co_3O_4$, which is similar to the previous observations in Karabela's research [46]. The morphology of the fast propagation zone becomes rougher as it expands. The final fracture zone also shows a classic crystallographic fracture formed by {1 1 1} facets.

Due to the different oxidation properties of individual specimens, the oxide layer thickness and the oxidation-induced crack depth (see Fig. 12**(b)**) of the OI mode are significantly higher than those of POI mode (see Fig. 9**(c)**), which indicates that the OI mode has a faster oxidation corrosion rate and can reach the propagation threshold of surface crack earlier. Compared with the PPI mode and POI mode, the porosity sizes on the fracture surface of the OI mode are smaller. These pore sizes may be smaller than the critical propagation size, so that the primary crack cannot initiate from the porosity defect. Therefore, only after more fatigue cycles can a large propagation zone be formed by the OI mode and lead to specimen fracture. The test results also show that under the same applied stress, the specimen of OI mode has the highest fatigue life compared to other initiation modes.

For OI mode, the surface oxidation induced crack will propagate to Region 3 until fracture (see Fig. 11). Since there are only five specimens of OI modes in all 48 specimens and the mechanism of OI mode is inconsistent with that of the porosity dominated fatigue life in this paper. The mechanism of OI initiation is not considered in the subsequent life prediction.

### 3.3. Defect-tolerance fatigue design

#### 3.3.1. Safe-life region

It can be seen from the fracture surface analysis that the large internal porosity defect is the main factor controlling the HCF life of NBSX superalloy. The Kitagawa-Takahashi (K-T) diagram connects the defect size with the fatigue limit in a semi empirical way by combining fatigue limit with the fracture mechanics, which has been used to determine a safe (infinite) life region and guide defect-tolerance fatigue design [7,29]. As shown in Fig. 15, the K-T diagram can be divided into safe life region ($N > 10^7$) and limited life region ($N < 10^7$) by horizontal and slanting lines. The horizontal line in the K-T diagram denotes the fatigue limit range $\Delta\sigma_{th}$ of near defect-free materials. From the test results, the

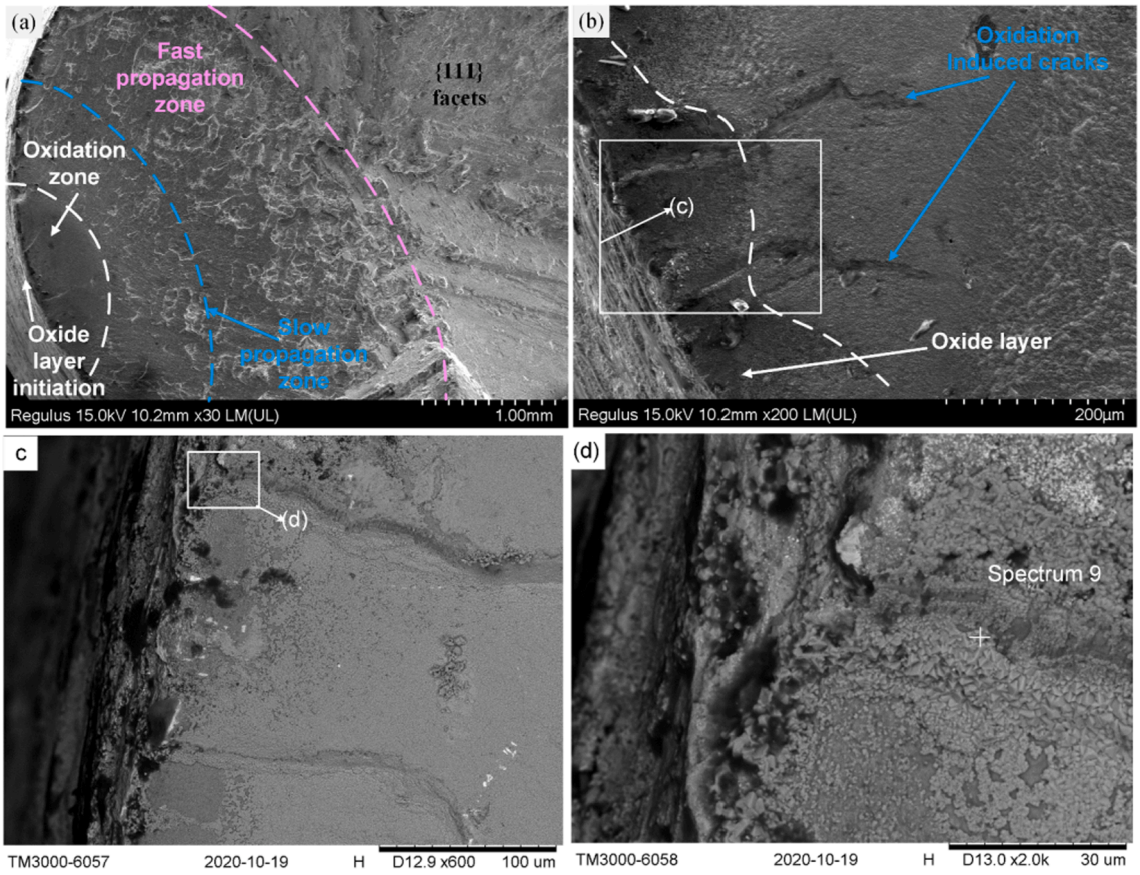


**Fig. 12.** Typical fracture surfaces of pure oxide layer initiation mode. (a) is the typical fracture surface, (b) is the surface propagation zone of (a), (c) and (d) are respectively the high magnification view of the oxidation-induced crack in (b) and (c).

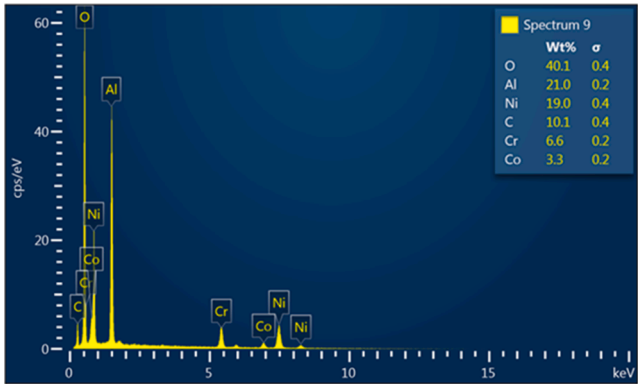


**Fig. 13.** The EDS results of the oxidation-induced crack and the scanning sites are marked in Fig. 12**(d)** [32].

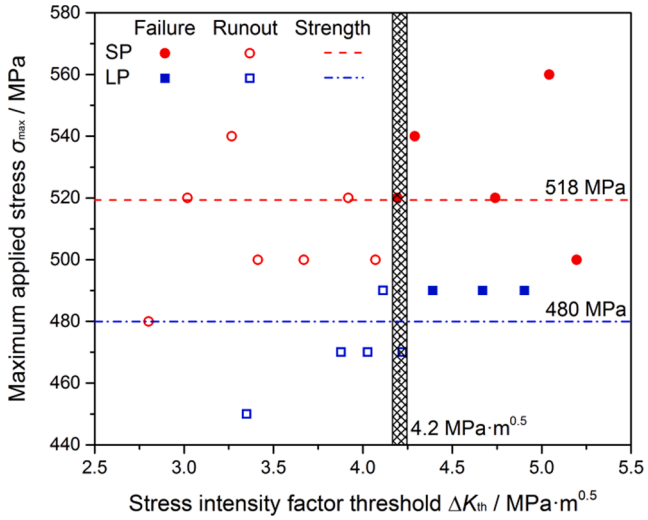


**Fig. 14.** Stress intensity factor threshold for the SP and LP specimens. To obtain the pore size, the survival specimens were then fatigued to fracture.

fatigue limits of the SP and LP groups are 518 MPa and 480 MPa respectively.

The stress intensity factor (SIF) range $\Delta K$ at the front of the critical pore defect can be expressed as [47,48],

$$\Delta K = Y\Delta\sigma\sqrt{\pi\phi_{surr}} \quad (1)$$

where $Y$ is the geometric correction factor. $Y = 0.65$ is for surface defects and $Y = 0.5$ is for internal defects. In this paper, the failure cracks all initiated from internal pores. $\Delta\sigma$ is the maximum applied stress and $\phi_{surr}$ is the critical pore size. It should be pointed out that $\phi_{surr}$ was originally proposed as the root mean square of the projected area of the defect$\sqrt{area}$. For circular defects, the size $\sqrt{area}$ is close to the diameter.

However, 2D metallographic image is often hard to obtain the real size of defects, whose results are usually smaller than the real size. Therefore, the Fret diameter (the circumscribed circle diameter of pore defect) is used to replace $\sqrt{area}$ for a more conservative result, which is an alternative practice in fatigue life prediction and proved to be reasonable [37,38]. According to Equation (1), the slanting line in K-T diagram can be described as a function of fatigue limit range$\Delta\sigma_{th}$, critical pore size $\phi_{surr}$ and the SIF threshold $\Delta K_{th}$ [28],

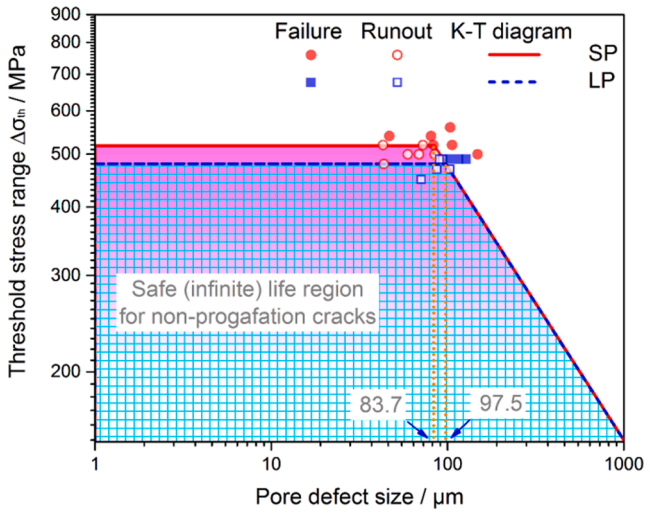


**Fig. 15.** Kitagawa-Takahashi diagrams of SP and LP specimens.

$$\Delta\sigma_{th} = \frac{\Delta K_{th}}{Y\sqrt{\pi\phi_{surr}}} \tag{2}$$

The SIF threshold $\Delta K_{th}$ can be obtained [49] by substituting the critical pore sizes (see Table 2 and Table 3) and corresponding maximum applied stress $\Delta\sigma$ into Equation (1). The calculated SIF for failure specimens and runout specimens are shown in Fig. 14. It should be pointed out that the SIF threshold calculated here is an equivalent SIF threshold, because the fundamental hypothesis of Equation (1) is that the defect is equivalent to a small crack. It can be seen that the SIF of failure specimens are higher than those of runout specimens. As the SIF threshold is a material constant and the materials of SP and LP specimens are the same, the SIF threshold for SP and LP specimens should be identical. Therefore, the SIF threshold can be determined by the boundary between all failure and runout specimens in spite of the specimen group (SP or LP specimens). Then the slanting line in the K-T diagrams of SP and LP groups can be obtained by substituting the SIF threshold $\Delta K_{th} = 4.2$ MP·m$^2$ into Equation (2).

In Fig. 15, the safe porosity sizes of SP and LP groups determined by the intersection of the horizontal line and slanting line in K-T diagrams are 83.7 μm and 97.5 μm respectively. Theoretically, the pore size lower than the safe threshold would not be expected to have a detrimental effect on the fatigue limit. However, above the safe threshold, the fatigue limit could drastically decrease with the increase of the pore size. The filling part below the curve is the safe-life region determined by non-propagating cracks. Conventionally, it is expected that the specimens within this region would have an infinite lifetime ($N > 10^7$). From the test results, the runout data of LP and SP groups are located in their respective safe-life regions, and their failure data are located outside their respective safe-life regions. This indicates that the original K-T diagram is also suitable for the defect-tolerance analysis of NBSX superalloy at high temperatures.

As the critical pore size of LP group is larger than that of SP group, the fatigue limit of LP group is lower than that of SP group. Therefore, the safe-life region in the K-T diagram of LP group is smaller than that of SP group. The practical fatigue design always choses the conservative results, so the K-T diagram of LP group is taken as the final result.

### 3.3.2. *Life prediction model in the finite-life region*

Although the internal large critical pores are the main factor restricting the HCF life of NBSX, the fatigue damage caused by oxidation cannot be ignored at low stress, especially near the fatigue limit. Therefore, the damage caused by the critical pores and the oxidation damage are considered in the fatigue life prediction model. The slow propagation zones of the internal crack and the oxidation-induced crack do not show obvious interconnection from the fracture surface of POI mode(see Fig. 7**(b)**), and the propagation depth of the oxidation-induced secondary crack is much smaller than the internal crack size. The increase of crack area reduces the bearing area of the specimen, which eventually leads to fracture. From this point of view, it seems that the internal crack and the oxidation-induced crack have no coupling effect. So the total fatigue damage $D$ can be expressed as the addition of the porosity damage $D_p$ and the oxidation damage $D_o$ [32,50,51],

$$D = D_p + D_o \tag{3}$$

(I) Porosity damage.

The NBSX superalloy is a typical face-centered cubic crystal, with four octahedral slip planes and three cubic slip planes, and damage parameters on the octahedral slip planes have a great influence on its fatigue life [52]. This is because the activation of the slip system is the reason for its plastic deformation [53]. The fracture surface analysis in Section 3.2 shows that the crack propagation path is perpendicular to the loading direction. However, microscopic researches [43,54,55] show that although the macroscopic crack is type mode I, the crack at the micro level initiation and zigzag propagation along the slip surface. Our previous study of DD5 [35] also found that clear intersecting slip traces around the pore defect, and the slip traces left on the fracture surfaces are consistent with the octahedral slip trace, which indicates that crystallographic slip along octahedral slip systems dominates the crack initiation process. Due to the natural critical plane (the slip plane), the multiaxial critical plane damage parameters are often used to evaluate the fatigue life of NBSX superalloy [3]. Fatemi et. al. [56] proposed a Fatigue Indicator Parameter (FIP), which is used to describe the formation and expansion of small cracks,

$$\mathrm{FIP} = \Delta\gamma^p_{max}\left[1 + k\frac{\sigma_n^{max}}{\sigma_y}\right] \tag{4}$$

In the FIP parameter, $\Delta\gamma^p_{max}$ is the maximum shear strain range and the slip plane where $\Delta\gamma^p_{max}$ located is defined as the critical plane. $\sigma_n^{max}$ is the maximum normal stress on the critical plane, $\sigma_y$ is the yield strength, and $k$ is a parameter with a value between 0.5 and 1.

The critical plane damage parameter FIP is used to evaluate fatigue life from the micro perspective. When applying the FIP parameter to the NBSX, Steuer et al. [41] reconsidered it to capture the crack initiation size, as shown in the following formula,

$$\mathrm{FIP} = \frac{\mu\Delta\sigma}{E_{[001]}}\left[1 + k\frac{\Delta K}{\Delta K_{threshold}}\right] \tag{5}$$

According to the elastic method, the applied stress range $\Delta\sigma$ is multiplied by Schmid factor $\mu$ to obtain the shear stress on the critical slip plane, and then divided by the modulus $E_{[001]}$ in [0 0 1] direction to obtain the maximum shear strain range$\Delta\gamma^p_{max}$. For the specimen with [0 0 1] orientation, the Schmid factor $\mu$ of critical slip plane is 0.408. The elastic modulus in [0 0 1] direction of SP group and LP group are 71.9 GPa and 72.9 GPa respectively [32]. To capture the pore size influence on crack initiation, the maximum normal stress $\sigma_n^{max}$ is replaced by the SIF range$\Delta K$, and the yield strength $\sigma_y$ is replaced by the SIF threshold$\Delta K_{threshold}$. The SIF range $\Delta K$ can be calculated by Equation (1), and according the analysis in section 3.3.1, the SIF threshold$\Delta K_{threshold} = 4.2$ MPa × m$^{0.5}$. To get better fitting result and general conclusion, the parameter $k$ is always taken as 1 [20,22,41].

Previous work [32] has shown that, for the specimens of PPI mode, their fatigue lives determined by porosity damage satisfy the power relationship with the FIP parameter,

$$\mathrm{FIP} = c \times (N_p)^d \tag{6}$$

where $c$ and $d$ are the fitting parameters, $N_p$ represents the fatigue life considering only porosity damage (without oxidation damage). The test data of the first three stress level (corresponding to the PPI mode) is used

to fit the FIP model, and the fitting results are shown in Fig. 16 ($c$ = 0.04427 and $d$ = -0.11969), where the FIP parameter is calculated by Equation (5). The good fitting result, on the one hand, is due to the fact that the SIF threshold test results is used, on the other hand, it shows that FIP parameter is indeed reasonable to describe pore damage. Then the porosity damage can be calculated by Equation (7), where $N_f$ represents the real fatigue life considering porosity damage and oxidation damage.

$$D_{\mathrm{p}} = \sum_{i=1}^{N_f} \frac{1}{N_{\mathrm{p}}} = \frac{N_f}{N_{\mathrm{p}}} \tag{7}$$

(II) Oxidation damage.

The thickness of oxide layer formed on the surfaces increased with the exposure time at high temperature [57,58]. The newly formed oxide layer can be broken and peeled off by cyclic loading, which exposes fresh surface to the air and high temperature again. Then the oxidation damage is induced along with the continuous repetition of the above mechanisms under cyclic loading. The depth of the oxidation-induced crack is close to that of the surface slow propagation zone, and the slow propagation life accounts for most of the fatigue life. Therefore, the oxidation damage is mainly related to the oxidation-induced crack depth. Then the oxidation damage can be defined as the ratio of the oxidation-induced crack depth $h$ to the critical depth of the oxidation-induced crack $h_{\mathrm{c}}$ [50],

$$D_o = \frac{h}{h_{\mathrm{c}}} \tag{8}$$

Since the depth of the oxidation induced crack is consistent with that of the slow propagation zone, and the slow propagation zone depth is easier to measure, the critical depth of oxidation-induced crack $h_{\mathrm{c}}$ can be obtained by the slow propagation zone depth of OI mode. The depth of the slow propagation zone under OI mode was measured, the measurement results are listed in Table 5, and the average value 1164.5 μm is taken as the critical depth of oxidation-induced crack $h_{\mathrm{c}}$.

The oxidation kinetic equation can be employed to calculate the oxidation-induced crack depth $h$, which follows the parabolic law [57],

$$h = \sqrt{A\Delta t} = \sqrt{A \cdot N_f / f} \tag{9}$$

where $\Delta t$ is the real fatigue time, which can be expressed by dividing the number of fatigue cycles $N_f$ by the loading frequency$f$. This reflects that the longer the fatigue time, the more severe the oxidation damage. $A$ is the oxidation rate constant, which can be determined by the Arrhenius equation [57,58],

**Table 5**
The maximum depth of oxidation-induced crack at pure oxide layer initiation mode.

| Reference | Maximum depth of oxidation -induced crack/μm | Mean value/μm |
|---|---|---|
| SP-9 | 1046.3 | 1164.5 |
| SP-13 | 1200.6 | |
| LP-10 | 1118.1 | |
| LP-18 | 1154.3 | |
| LP-20 | 1303.4 | |

$$A = A_{\mathrm{o}} e^{-\frac{Q_{\mathrm{O}}}{RK}} \tag{10}$$

where $A_{\mathrm{o}}$ is the pre-exponential factor, $Q_{\mathrm{o}}$ is the activation energy for oxidation, $R$ is the universal gas constant, and $K$ is the Kelvin temperature. The pre-exponential factor $A_{\mathrm{o}}$ and activation energy $Q_{\mathrm{o}}$ for oxidation can be found in Ref. [58], where $A_{\mathrm{o}} = 10^{-4}$ m$^2$/s and$Q_{\mathrm{o}}$ = 168.5 kJ/mol.

(III) Model evaluation.

The expressions of porosity damage and oxidation damage have been given previously, so the total fatigue damage $D$ can be expressed as,

$$D = D_{\mathrm{p}} + D_{\mathrm{o}} = \frac{N_f}{N_{\mathrm{p}}} + \frac{h}{h_c} \tag{11}$$

When the total fatigue damage is equal to the critical damage, the fatigue failure occurs. The critical damage is usually set as 1. The influence of porosity size and oxidation on the HCF life of NBSX has been always considered in Equation (11), which does not specifically distinguish the PPI mode and POI mode. The reason is that the oxidation damage increases with the increase of fatigue time, and the fatigue time of PPI mode is very short. The calculated oxidation damage of PPI mode is very small and can be ignored.

Fig. 17 compares the predicted life with the experimental life. It can be seen that most of the predicted results are within the 2-time scatter band, and only three data are located in the 2.5-times scatter band. In this paper, not all experimental data are used to obtain model parameters. The SIF threshold value was calculated from the critical pore size and applied stress by 20 specimens near fatigue limit (including 7 unbroken specimens) in Fig. 14, and their fatigue life data is not used, which has little impact on the evaluation of model scatter. Only the fatigue life of 17 specimens under high stress were used to fit the FIP model in Fig. 16, and these specimens are different from those in Fig. 15. However, the fatigue life model was evaluated using the test data of all

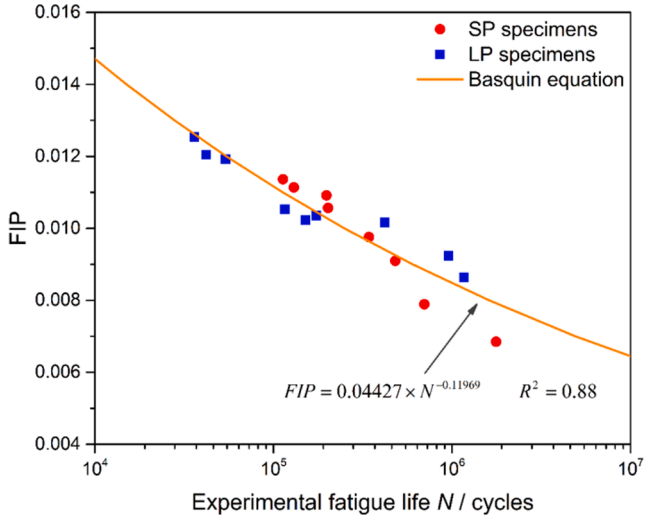


**Fig. 16.** FIP versus the experimental fatigue life for specimens of pure pore defects initiating failure cracks.

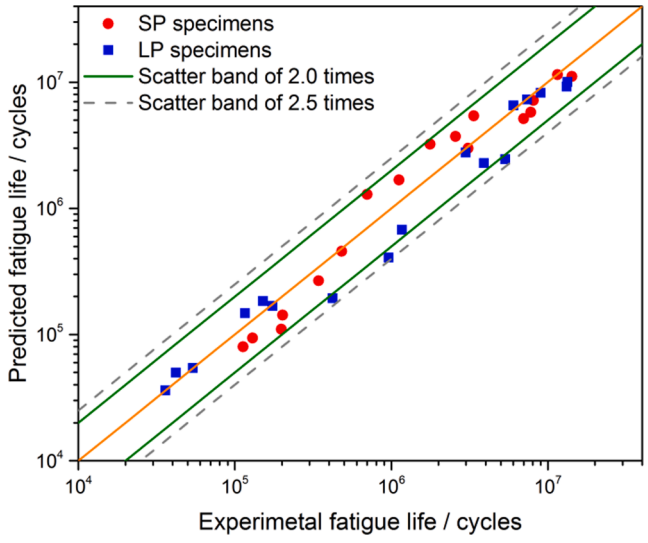


**Fig. 17.** Fatigue life prediction results compared with the experimental results.

41 fracture specimens. Therefore, the evaluation results of the model are reliable. Evaluation result reflects that the proposed life prediction model in this paper can effectively and accurately evaluate the effect of porosity size and oxidation on the HCF life of NBSX superalloy.

The life distribution is depicted by the contour plots and then an extended K-T diagram is plotted in Fig. 18. This extended K-T diagram considers not only the infinite life region determined by the K-T diagram but the defect-determined residual life distribution by Equation (11) within the finite life region, which is an attempt to guide the defect-tolerance fatigue design of the NBSX blade in engineering. However, it must be pointed out that the life model and the K-T diagram in this paper are proposed in HCF stage, the LCF region in Fig. 18 are only used for reference.

### 3.4. Fatigue limit evaluation

(I) The effect of porosity size.

It is time-consuming and laborious to determine the fatigue limit of NBSX superalloy by experiment, and a relatively fast and effective method is needed to evaluate its fatigue limit in engineering. Murakami's work shows that the fatigue limit of materials is always related to the non-propagating crack associated with the defect size, so he proposed a fatigue limit evaluation model corresponding to macro type I crack from the perspective of non-propagating crack [27]. The Murakami model is simple and effective as it only requires the hardness and maximum pore size of materials, and has been widely used to evaluate the effect of defect size on fatigue limit.

However, the Murakami model is an empirical estimation of the fatigue limit from HV measurements for polycrystalline materials at ambient temperature. Although the model is proposed by results of polycrystalline materials, it is summarized from experience and is not necessarily only applicable to polycrystalline materials. So we try to apply the model to NBSX at high temperature in this paper. For PPI mode, the fracture surface is macro type I crack and the fatigue damage is closely related to the porosity size. Therefore, the Murakami model is used to evaluate the fatigue limit from the macro perspective. The SIF threshold $\Delta K_{\mathrm{th}}$ of pore defect at a stress ratio of $-1$ can be estimated by the hardness and maximum pore size [5],

$$\Delta K_{\mathrm{th}} = g\cdot(\mathrm{HV}+120)\cdot(\phi_{\mathrm{surr}})^{1/3} \tag{12}$$

where the critical pore location is considered by a corrective factor, $g = 3.3\times10^{-3}$ is for surface pore and $g = 2.77\times10^{-3}$ is for internal pore. HV is the Vickers hardness, which is 455.5 kgf/mm$^2$ and 448.9 kgf/mm$^2$ respectively for the SP group and LP group. $\phi_{surr}$ is the estimated maximum pore size, which is 153 μm and 231 μm respectively for the SP group and LP group. Assume that the SIF range as the driving force of the crack is equal to the SIF threshold as the resistance,$\Delta K = \Delta K_{th}$. Thus, the fatigue limit $\sigma_{\mathrm{th\,-\,p}}$ that only considers the porosity defect can be estimated from Equation (1) and Equation (12),

$$\sigma_{\mathrm{th\,-\,p}} = \frac{C\cdot(\mathrm{HV}+120)}{(\phi_{\mathrm{surr}})^{1/6}} \tag{13}$$

where $C$ is a position corrective factor, $C = 1.43$ for surface pore and $C = 1.56$ for internal pore.

The Equation (12) is put forward in the stress ratio of $-1$, but the tension–tension HCF tests in this paper is under the stress ratio of 0.1. So the average stress needs to be considered. Koutiri et al. [59] found that the SIF threshold under different stress ratios satisfies Equation (14),

$$\frac{\Delta K_{\mathrm{th}}^{R}}{\Delta K_{\mathrm{th}}^{R=0}} = \frac{1-R}{1-\kappa R} \tag{14}$$

where $\kappa$ is a material parameter, $\Delta K_{\mathrm{th}}^{R=0}$ and $\Delta K_{\mathrm{th}}^{R}$ are respectively the SIF threshold under the stress ratio of 0 and $R$. Then the Equation (13) can be modified by the average stress,

$$\sigma_{\mathrm{th\,-\,p}}(R) = \frac{C\cdot(\mathrm{HV}+120)}{(\phi_{\mathrm{surr}})^{1/6}}\cdot\frac{1-R}{1-\kappa R}\cdot\frac{1+\kappa}{2} \tag{15}$$

The fatigue limit evaluation model above can only predict the fatigue limit in PPI mode because it only considers the material hardness, the porosity defect size and the stress ratio. The predicted results should be consistent with the reference fatigue limit of PPI mode (see Table 4). Due to the lack of experimental data under different stress ratios, the material constant $\kappa$ can be obtained by substituting the reference fatigue limit 576 MPa and other material parameters of SP group into Equation (15). The calculation result of the material parameter $\kappa$ is 0.43. Then the fatigue limit of LP group in PPI mode can be estimated by Equation (15). The estimated reference fatigue limit for LP group is 536 MPa, which is very close to the experimental reference fatigue limit of 534 MPa. This reflects that the Murakami model modified by the average stress can evaluate the effect of the porosity size on the fatigue limit for NBSX superalloy well.

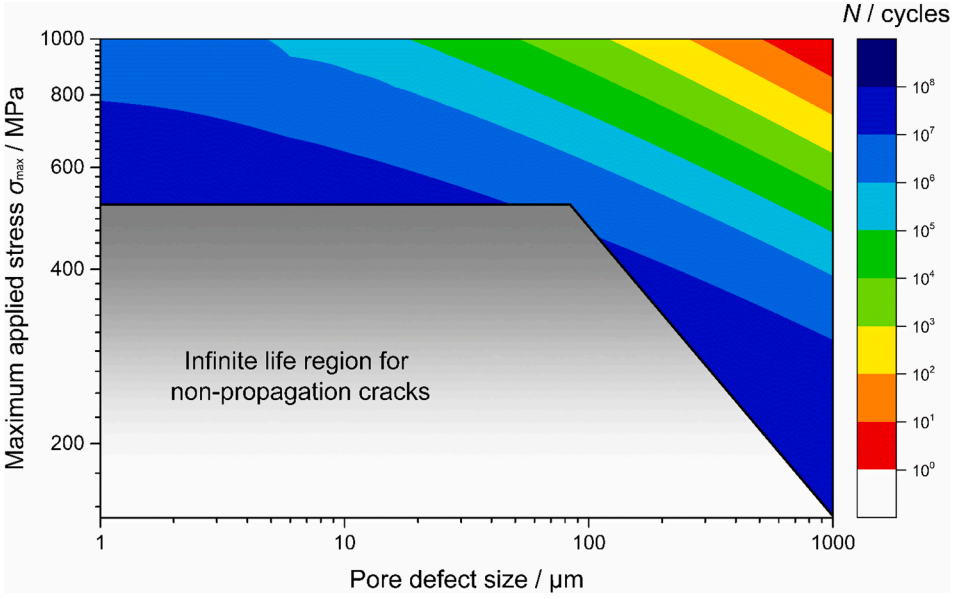


**Fig. 18.** Extended Kitagawa-Takahashi diagram involving both infinite (safe) life region and the defect-determined fatigue life distribution in the finite life region.

(II) The effect of porosity size and oxidation.

The experimental results show that the real fatigue limit is not only related to porosity size, but also weakened by oxidation damage. Therefore, to predict the real fatigue limit of NBSX at high temperatures, both porosity defect and oxidation should be considered. As the Equation (15) has been proven effective to evaluate the effect of the porosity size on the fatigue limit, an oxidation correction factor will be further considered on the basis of Equation (15) to add the effect of oxidation on the fatigue limit.

According to Table 4, the S-N curve of PPI mode satisfies the power law$\sigma_{\max} = a \times N^b$. It is assumed that the fatigue life corresponding to the fatigue limit is $10^7$ cycles. Then, when only considering the effect of porosity size on fatigue limit$\sigma_{\text{th - p}}$, the total damage can be expressed by Equation (7),

$$D = D_{\text{p}} = \sum_{i=1}^{N_f=10^7} \frac{1}{N_{\text{p}}} = \frac{N_{\text{f}} = 10^7}{N_{\text{p}}} = \frac{10^7}{\left(\sigma_{\text{th - p}}/a\right)^{1/b}} = 1 \tag{16}$$

When considering the effect of porosity size and oxidation on fatigue limit$\sigma_{\text{th - po}}$, the total damage can be expressed by Equation (11),

$$D = D_{\text{p}} + D_{\text{o}} = \frac{10^7}{\left(\sigma_{\text{th - po}}/a\right)^{1/b}} + D_{\text{o}}\left(N_f = 10^7\right) = 1 \tag{17}$$

Define the oxidation correction factor$O$,

$$O = \frac{\sigma_{\text{th - po}}}{\sigma_{\text{th - p}}} \tag{18}$$

Then combining Equation (16) and Equation (17), the oxidation correction factor can be calculated by:

$$O = \left[1 - D_{\text{o}}\left(N_f = 10^7\right)\right]^{-b} \tag{19}$$

where the oxidation correction factor $O$ is associated with the index $b$ of the S-N curve in PPI mode and the oxidation damage at$N_f = 10^7$. It can be seen from Table 4, the index $b$ of the S-N curve in PPI mode for the same NBSX with different porosity size is the same, so the index $b$ could be considered as a material constant. The oxidation damage at $N_f = 10^7$ is also a fixed value, which can be calculated by Equation (8). Therefore, the oxidation correction factor proposed in this paper is a constant which is independent of the pore size and can be calculated from the material constants. Under the investigated conditions in this paper, the calculation result of the oxidation correction factor is$O = 0.902$. According to Equation (15), Equation (18) and Equation (19), the fatigue limit evaluation model that considers porosity size and oxidation can be proposed,

$$\sigma_{\text{th - po}}(R) = \frac{O \cdot C \cdot (\text{HV} + 120)}{(\phi_{\text{surr}})^{1/6}} \cdot \frac{1 - R}{1 - \kappa R} \cdot \frac{1 + \kappa}{2} \tag{20}$$

The predicted fatigue limits are 523 MPa and 483 MPa respectively, which are very close to the experimental results of 518 MPa and 480 MPa respectively, and the relative error is less than 1%. This reflects that the fatigue limit prediction model in this paper can accurately predict the fatigue limit of NBSX, considering the porosity size and oxidation. Besides, the model parameters are easy to obtain and the oxidation correction factor can be calculated explicitly by material parameters, which is convenient for engineering applications.

## 4. Conclusions

In this paper, two kinds of second-generation NBSX superalloy DD5 with different porosity sizes were adopted to investigate the influence of pore size and oxidation on the fatigue properties ($T = 980°C$,$f = 110$ Hz, and $R = 0.1$). Combined with the previous research results, a complete HCF S-N curve was given, and the crack initiation mode was analyzed. On this basis, an HCF life prediction model considering the pore size and oxidation was proposed, and the defect-tolerance design was carried out based on the extended K-T diagram. Finally, based on the Murakami model, a fatigue limit prediction model considering the average stress and oxidation correction was put forward to evaluate the effect of porosity size and oxidation on the fatigue limit of NBSX superalloy. The following conclusions can be drawn from this research:

(1) Under the investigated conditions, the S-N curve shows a three-stage characteristic in the double logarithmic coordinate. The first stage is a long straight descent line, followed by a short and sharp descent transition stage, and the third stage is a straight descent line again. Fractography analysis shows that the characteristics of the S-N curve is due to the transition of crack initiation mode. The linear stage under high stress is dominated by pure porosity initiation (PPI) mode, while the linear stage under low stress is dominated by porosity and oxide layer co-initiation (POI) mode. In the middle transition, with the decrease of stress, the PPI mode gradually transits to the POI mode.

(2) Damage caused by large pore defects is the main reason that controls HCF life. Under the same stress level, the fatigue life of the specimens with larger pores is generally lower than that of specimens with smaller pores. Oxidation damage is related to the real time of fatigue. The longer the fatigue time, the greater the oxidation damage. The porosity damage is considered based on the critical plane damage parameter, and the oxidation damage is expressed by the oxidation kinetic equation. Then, an HCF life prediction model considering the pore size and oxidation was proposed. The prediction results show that the proposed life prediction model can effectively and accurately evaluate the effect of porosity size and oxidation on the HCF life.

(3) The runout data of specimens are located in the safe-life regions of the K-T diagram, while the failure data are located outside the safe-life regions. This indicates that the original K-T diagram is also suitable for the defect-tolerance analysis of NBSX superalloy at high temperatures. Combined with the life prediction model in this paper, an extended K-T diagram is given for defect-tolerance analysis, including infinite (safe) life region and the defect-determined fatigue life distribution in the finite life region.

(4) The Murakami model can evaluate the influence of pore size on the reference fatigue limit of NBSX superalloys. However, the real fatigue limit is not only related to porosity size, but also weakened by oxidation damage. Based on the Murakami model, a fatigue limit prediction model considering the porosity size and oxidation was proposed. The model is easy to calculate, accurate in prediction, and suitable for engineering applications.

*CRediT authorship contribution statement*

**Wen Jiang:** Conceptualization, Methodology, Software, Validation, Writing – original draft, Writing – review & editing, Visualization, Funding acquisition. **Piao Li:** Conceptualization, Methodology, Validation, Writing – review & editing, Visualization. **Wei-Xing Yao:** Resources, Supervision, Project administration, Funding acquisition. **Shao-Shi Rui:** Investigation, Formal analysis, Writing – review & editing. **Hui-Ji Shi:** Resources, Supervision. **Jie Huang:** Funding acquisition, Formal analysis.

## Declaration of Competing Interest

The authors declare that they have no known competing financial interests or personal relationships that could have appeared to influence the work reported in this paper.

## Acknowledgements

This work was supported by the National Major Science and Technology Project of China (2017-VI-0003-0073), the National Natural Science Foundation of China (Grant No. 52075244 and No. 52002181), the Priority Academic Program Development of Jiangsu Higher Education Institutions (Grant No. 1108007002). Dr. Yanhong Yang and Dr. Yizhou Zhou from the Institute of Metal Research, Chinese Academy of Science, are greatly appreciated for providing the DD5 NBSX superalloys.

## References

[1] I.S. Kim, B.G. Choi, J.E. Jung, J. Do, C.Y. Jo, Effect of microstructural characteristics on the low cycle fatigue behaviors of cast Ni-base superalloys, Mater. Charact. 106 (2015) 375–381.
[2] L. Liu, J. Meng, J.-L. Liu, H.-F. Zhang, X.-D. Sun, Y.-Z. Zhou, Effects of crystal orientations on the low-cycle fatigue of a single-crystal Nickel-based superalloy at 980 C, Acta Metallurgica Sinica (English Letters) 32 (3) (2019) 381–390.
[3] P. Li, W. Yao, H. Shi, et al., A topologized resolved shear stress method for the life prediction of Nickel-base single crystal superalloys, Theor. Appl. Fract. Mec. 108 (2020), 102624.
[4] M. Moalla, K.H. Lang, D. Löhe, The fatigue behavior of NiCr22Co12Mo9 under low-frequency thermal-mechanical loading and superimposed higher-frequency mechanical loading, Thermomech. Fatigue Behav. Mater. 4 (2003) 195–209.
[5] B.A. Cowles, High cycle fatigue in aircraft gas turbines—an industry perspective, Int. J. Fract. 80 (2–3) (1996) 147–163.
[6] Y. Murakami, Metal Fatigue-effects of small defects and nonmetallic inclusions, Oxford, 2002.
[7] U. Zerbst, M. Madia, M. Vormwald, et al., Fatigue strength and fracture mechanics – a general perspective, Eng. Fract. Mech. 198 (2018) 2–23.
[8] Y. Hong, X. Liu, Z. Lei, C. Sun, The formation mechanism of characteristic region at crack initiation for very-high-cycle fatigue of high-strength steels, Int. J. Fatigue 89 (2016) 108–118.
[9] T.A. Gordeeva, R.A. Dul'nev, T.V. Rybina, G.I. Sobolev, V.A. Chumakov, N. F. Shvanova, Thermal fatigue strength of directionally solidified, casting Nickel alloy ZhS6U, Strength Mater. 9 (10) (1977) 1181–1188.
[10] M.A. Gorbovets, M.S. Belyayev, P.V. Ryzhkov, Fatigue strength of heat-resistant Nickel alloys produced by selective laser melting, Aviation Mater. Technol. (3) (2018) 50–55.
[11] J.H. Zhang, Y.B. Xu, Z.G. Wang, Z.Q. Hu, Fatigue behavior of a single crystal Nickel-base superalloy, Scr. Metall. Mater. 32 (12) (1995) 2093–2098.
[12] Kevinsanny, S. Okazaki, O. Takakuwa, Y. Ogawa, Y. Funakoshi, H. Kawashima, S. Matsuoka, H. Matsunaga, Defect tolerance and hydrogen susceptibility of the fatigue limit of an additively manufactured Ni-based superalloy 718, Int. J. Fatigue 139 (2020) 105740.
[13] H. Lin, H.P. Geng, Y.Y. Zhang, H. Li, X.Y. Liu, X.F. Zhou, L. Yu, Fatigue strength and life prediction of a MAR-M247 nickel-base superalloy gas turbine blade with multiple carbide inclusions, Strength Mater. 51 (1) (2019) 102–112.
[14] W. Ren, T. Nicholas, Effects and mechanisms of low cycle fatigue and plastic deformation on subsequent high cycle fatigue limit in Nickel-base superalloy Udimet 720, Mater. Sci. Eng. A 332 (1) (2002) 236–248.
[15] C. Zhaokuang, Y.u. Jinjiang, S. Xiaofeng, G. Hengrong, H.u. Zhuangqi, High cycle fatigue behavior of a directionally solidified Ni-base superalloy DZ951, Mater. Sci. Eng. A 496 (1-2) (2008) 355–361.
[16] L. Shui, T. Jin, Sun Xf, Hu Zq, High-cycle fatigue behavior of AM3 Nickel-base single crystal superalloy at high temperature, Int. J. Mod. Phys. B 24 (2012) 2886–2891.
[17] H. Wang, C. Yuan, J.T. Guo, et al., High cycle fatigue behavior of a wrought Nickel-base superalloy GH4698, Mater. Sci. Forum 788 (2014) 414–420.
[18] M. Filippini, Notched fatigue strength of single crystals at high temperature, Procedia Eng. 10 (2011) 3787–3792.
[19] Z. Liqiong, L. Yilong, Y. Zhen, et al., Effect of shot peening on high cycle fatigue limit of FGH4097 P/M superalloys at room temperature, Rare Metal Mat. Eng. 47 (7) (2018) 2198–2204.
[20] L.M. Bortoluci Ormastroni, L. Mataveli Suave, A. Cervellon, P. Villechaise, J. Cormier, LCF, HCF and VHCF life sensitivity to solution heat treatment of a third-generation Ni-based single crystal superalloy, Int. J. Fatigue 130 (2020) 105247.
[21] A. Cervellon, S. Hémery, P. Kürnsteiner, et al., Crack initiation mechanisms during very high cycle fatigue of Ni-based single crystal superalloys at high temperature, Acta. Mater. 188 (2020) 131–144.
[22] A. Cervellon, J. Cormier, F. Mauget, Z. Hervier, Y. Nadot, Very high cycle fatigue of Ni-based single-crystal superalloys at high temperature, Metall. Mater. Trans. A 49 (9) (2018) 3938–3950.
[23] A. Cervellon, J. Cormier, F. Mauget, Z. Hervier, VHCF life evolution after microstructure degradation of a Ni-based single crystal superalloy, Int. J. Fatigue 104 (2017) 251–262.
[24] M. Lamm, R.F. Singer, The effect of casting conditions on the high-cycle fatigue properties of the single-crystal Nickel-base superalloy PWA 1483, Metall. Mater. Trans. A 38 (6) (2007) 1177–1183.
[25] A. Karabela, L.G. Zhao, B. Lin, et al., Oxygen diffusion and crack growth for a nickel-based superalloy under fatigue-oxidation conditions, Mater. Sci. Eng. A 567 (2013) 46–57.
[26] G. Calvarin-Amiri, A.M. Huntz, R. Molins, Effect of an applied stress on the growth kinetics of oxide scales formed on Ni-20Cr alloys, High Temperature Technol. 18 (2) (2001) 91–99.
[27] Y. Murakami, Material defects as the basis of fatigue design, Int. J. Fatigue 41 (2012) 2–10.
[28] Y.N. Hu, S.C. Wu, Z.K. Wu, et al., A new approach to correlate the defect population with the fatigue life of selective laser melted Ti-6Al-4V alloy, Int. J. Fatigue 136 (2020), 105584.
[29] E. Pessard, D. Bellett, F. Morel, et al., A mechanistic approach to the Kitagawa-Takahashi diagram using a multiaxial probabilistic framework, Eng. Fract. Mech. 109 (2013) 89–104.
[30] J. Tenkamp, A. Koch, S. Knorre, U. Krupp, W. Michels, F. Walther, Defect-correlated fatigue assessment of A356–T6 aluminum cast alloy using computed tomography based Kitagawa-Takahashi diagrams, Int. J. Fatigue 108 (2018) 25–34.
[31] M. Segersäll, D. Leidermark, J.J. Moverare, Influence of crystal orientation on the thermomechanical fatigue behaviour in a single-crystal superalloy, Mater. Sci. Eng. A 623 (2015) 68–77.
[32] W. Jiang, P. Li, W.-X. Yao, S.-S. Rui, H.-J. Shi, J. Huang, The effect of porosity size on the high cycle fatigue life of nickel-based single crystal superalloy at 980 C, Int. J. Fatigue 147 (2021) 106191.
[33] S. Hu, L. Liu, W. Yang, D. Sun, M. Huo, T. Huang, J. Zhang, H. Su, H. Fu, Formation of accumulated misorientation during directional solidification of Ni-based single-crystal superalloys, Metall. Mater. Trans. A 50 (4) (2019) 1607–1610.
[34] M.H. Raza, A. Wasim, S. Hussain, M. Sajid, M. Jahanzaib, Grain selection and crystal orientation in single-crystal casting: state of the art, Cryst. Res. Technol. 54 (2) (2019) 1800177.
[35] P. Li, W. Jiang, S.-S. Rui, W.-X. Yao, H.-j. Shi, Q.-N. Han, J. Huang, Effect of misorientation on the fatigue life of nickel-base single crystal superalloy DD5 at 980 C, Int. J. Fatigue 153 (2021) 106479.
[36] K. Xu, G. Wang, J. Liu, et al., Creep behavior and a deformation mechanism based creep rate model under high temperature and low stress condition for single crystal superalloy DD5, Mater. Sci. Eng. A 786 (2020), 139414.
[37] G. Nicoletto, R. Konečná, S. Fintova, Characterization of microshrinkage casting defects of Al–Si alloys by X-ray computed tomography and metallography, Int. J. Fatigue 41 (2012) 39–46.
[38] Q.G. Wang, P.E. Jones, Prediction of fatigue performance in aluminum shape castings containing defects, Metall. Mater. Trans. B 38 (4) (2007) 615–621.
[39] Y. Murakami, S. Beretta, Small defects and inhomogeneities in fatigue strength: experiments, models and statistical implications, Extremes 2 (2) (1999) 123–147.
[40] W.J. Dixon, A.M. Mood, A method for obtaining and analyzing sensitivity Data, J. Am. Stat. Assoc. 43 (241) (1948) 109–126.
[41] S. Steuer, P. Villechaise, T.M. Pollock, et al., Benefits of high gradient solidification for creep and low cycle fatigue of AM1 single crystal superalloy, Mater. Sci. Eng. A 645 (2015) 109–115.
[42] M.M. Kirka, K.A. Brindley, R.W. Neu, et al., Influence of coarsened and rafted microstructures on the thermomechanical fatigue of a Ni-base superalloy, Int. J. Fatigue 81 (10) (2015) 191–201.
[43] R.W. Neu, Crack paths in single-crystal Ni-base superalloys under isothermal and thermomechanical fatigue, Int. J. Fatigue 123 (2019) 268–278.
[44] P.K. Wright, M. Jain, D. Cameron, High cycle fatigue in a single crystal superalloy: time dependence at elevated temperature, Superalloys (2004).
[45] Z. Zhao, Q. Li, F. Zhang, et al., Transition from internal to surface crack initiation of a single-crystal superalloy in the very-high-cycle fatigue regime at 1100 C, Int. J. Fatigue 150 (2021), 106343.
[46] A. Karabela, L.G. Zhao, J. Tong, et al., Effects of cyclic stress and temperature on oxidation damage of a nickel-based superalloy, Mater. Sci. Eng. A 528 (19–20) (2011) 6194–6202.
[47] Y. Murakami, S. Kodama, S. Konuma, Quantitative evaluation of effects of non-metallic inclusions on fatigue strength of high strength steels. I: basic fatigue mechanism and evaluation of correlation between the fatigue fracture stress and the size and location of non-metallic inclusions, Int. J. Fatigue 11 (5) (1989) 291–298.
[48] Y. Murakami, H. Usuki, Quantitative evaluation of effects of non-metallic inclusions on fatigue strength of high strength steels. II: fatigue limit evaluation based on statistics for extreme values of inclusion size, Int. J. Fatigue 11 (5) (1989) 299–307.
[49] R. González, D.I. Martínez, J.A. González, et al., Experimental investigation for fatigue strength of a cast aluminium alloy, Int. J. Fatigue 33 (2) (2011) 273–278.
[50] D. Li, D. Shang, L. Xue, et al., Real-time damage evaluation method for multiaxial thermo-mechanical fatigue under variable amplitude loading, Eng. Fract. Mech. 229 (2020), 106948.
[51] F. Li, D. Shang, C. Zhang, et al., Thermomechanical fatigue life prediction method for nickel-based superalloy in aeroengine turbine discs under multiaxial loading, Int. J. Damage Mech. 28 (9) (2019) 1344–1366.
[52] Y. Su, Q. Han, C. Zhang, et al., Effects of secondary orientation and temperature on the fretting fatigue behaviors of Ni-based single crystal superalloys, Tribol. In.t 130 (2019) 9–18.
[53] W. Jiang, W. Yao, P. Li, et al., A fatigue life prediction method distinguishing fracture modes for Ni-based single crystal superalloys considering porosity defect, Theor. Appl. Fract. Mec. 112 (2021), 102883.

[54] S. Suzuki, M. Sakaguchi, H. Inoue, Temperature dependent fatigue crack propagation in a single crystal Ni-base superalloy affected by primary and secondary orientations, Mater. Sci. Eng. A 724 (2018) 559–565.
[55] P. Reed, I. Sinclair, X.D. Wu, Fatigue crack path prediction in UDIMET 720 Nickel-based alloy single crystals, Metall. Mater. Trans. A 31 (2000) 109–123.
[56] A. Fatemi, D.F. Socie, A critical plane approach to multiaxial fatigue damage including out-of-phase loading, Fatigue Fract. Eng. Mater. Struct. 11 (3) (1988) 149–165.
[57] X. Wu, Z. Zhang, A mechanism-based approach from low cycle fatigue to thermomechanical fatigue life prediction, J. Eng. Gas Turbines Power 138 (7) (2016) 72503.
[58] L.G. Zhao, J. Tong, M.C. Hardy, Prediction of crack growth in a Nickel-based superalloy under fatigue-oxidation conditions, Eng. Fract. Mech. 77 (6) (2010) 925–938.
[59] I. Koutiri, D. Bellett, F. Morel, et al., A probabilistic model for the high cycle fatigue behaviour of cast aluminium alloys subject to complex loads, Int. J. Fatigue 47 (2013) 137–147.